NMR Cryoporometry of Porous Materials and Articular Cartilage Models

Pro Gradu Thesis
Katja Tolkkinen
Physics Degree Program
NMR Research Unit
University of Oulu
2021

Acknowledgements

I would like to thank Postdoctoral Researcher Sarah Mailhiot for her support and guidance throughout the research and writing of this master's thesis. I am very grateful that she shared her research project with me and taught me how to work in the NMR laboratory. This master's thesis would not have been possible without her.

I am grateful to my supervisor Professor Ville-Veikko Telkki for guidance and for offering the opportunity to work in the NMR Research Group during my studies.

Abstract

Articular cartilage is one of the most studied porous biomaterial. It is an essential part of the human body because it makes the movement of the joint smooth and painless. The health of articular cartilage depends on its protein content, pore size and water components and these factors are directly related to progressive cartilage degeneration. Research of articular cartilage is important for development of early diagnosis, prevention and treatment of articular cartilage diseases.

Nuclear magnetic resonance cryoporometry is a non-invasive method for determining pore size distributions of porous materials. The aim of this thesis was to perform ^{1}H NMR cryoporometry on salt solutions, porous materials and articular cartilage hydrogels which were very simplified models of articular cartilage protein content. The cartilage gels were composed of collagen, proteoglycans and phosphate-buffered saline. Salt solutions as thermoporometric probe fluids have not been studied extensively and thus the phase transitions of saline and phosphate-buffered saline were studied. The results obtained from the cryoporometry experiments of salt solutions and porous silica gels were used to interpret the results of protein gel experiments. The end goal of the experiments was to estimate the pore size distributions of protein gels, identify which protein components water is associated with in articular cartilage, and measure the associated T_2 relaxation times.

As a result, it was observed that there occur two separate phase transitions in salt solutions during melting: the eutectic phase transition and the bulk melting. It was also found that both transitions occur over a certain temperature range instead of one specific temperature. Cryoporometry of silica gels imbibed with water or saline showed that the melting behaviour of solutions were different which also affected the computed pore size distributions. In conclusion, NMR cryoporometry of salt solutions is complex and traditional data interpretation cannot be applied.

The study of articular cartilage gels showed that the eutectic transition of phosphate-buffered saline and the wide temperature range of bulk melting caused additional peaks in the pore size distributions. By performing data analysis with two different methods, the peaks associated with both proteins were identified and pore size distribution was estimated to be approximately 2-5 nm. However, completely accurate information on pore size could not be determined by this method. T_2 relaxation time measurements showed that T_2 is dependent on the amount of collagen but not on the amount of proteoglycans at room temperature.

Contents

Chapter 1

Introduction

Articular cartilage is the specialized connective tissue covering the ends of the bones. The purpose of articular cartilage is to facilitate smooth, lubricated and painless movement of the joint. Osteoarthritis, a degenerative joint disease, is the most common musculoskeletal disorder worldwide affecting 10-12 % of the world population and the number continues to rise due to increasing age and obesity [1,2]. In 1743, Scottish physician William Hunter stated: "an ulcerated cartilage is a troublesome problem and once destroyed, it never repairs" [3]. Despite centuries of research, articular cartilage is still not fully understood and therapies for the end-stage osteoarthritis are very limited. Today, the most common form of treatment is the surgical joint replacement which is a major medical and economical problem. Research on articular cartilage is important in order to develop new potential therapies and diagnostics for joint diseases [2,4].

Nuclear magnetic resonance (NMR) spectroscopy provides many advantages on biological research because it is non-invasive. NMR utilizes non-invasive radio frequency radiation and measures signal from hydrogen found in water and proteins. The first NMR signal was detected in 1945 and today the application of NMR as clinical magnetic resonance imaging is the most widely used diagnostic method for articular cartilage diseases [5,6]. Water is a necessary component of articular cartilage enabling lubrication and nutrient transport by diffusion [1,4]. Injuries and degradation of articular cartilage have impact on the protein content, pore size distribution and amount of water in cartilage matrix. Hence, the study of cartilage porosity and water components may provide opportunities for understanding cartilage function, structure and conditions of osteoarthritis [1,2,7,8].

Characterization of porosity is a growing field of research due to the vast quantity of porous materials in nature, biological systems, industry and technology. Synthesized porous silica is one of the most studied porous material due to its highly ordered pore sizes and pore morphologies. NMR cryoporometry is a non-invasive method for measuring pore size distributions of porous materials based on the detection of melting point depression of confined liquid. In addition to measure pore size distribution, cryoporometry is a versatile method for providing information on properties of pore-filling liquid. NMR cryoporometry is one of the few thermoporometric methods capable of measuring pore sizes of wet samples and for that reason, it is a very advantageous method for studying biological materials [9,10]. However, salt solutions which commonly appear in biological systems have not been systematically studied as thermoporometric probe fluids, which poses challenges to cryoporometry of biological materials.

The purpose of this study was to investigate protein-associated water, pore size, and T_2 relaxation of articular cartilage models by proton NMR cryoporometry. First, the NMR cryoporometry set-up was tested on salt solutions and ordered silica beads to study the phase transitions of water and saline and to ensure that the method was able to distinguish different pore sizes. Finally, the NMR cryoporometry experiments were carried out on protein hydrogels of different protein concentrations.

The outline of this thesis consists of theoretical and experimental parts. In Chapters 2-5, there are introduced the basics of NMR phenomenon and NMR experiments, theory of NMR cryoporometry, structure and function of articular cartilage and basics of salt solutions as cryoporometric solvents. The samples, hardware, experiments and results are represented in Chapter 6. In Chapter 7, the results are discussed and the possibilities of the method used are considered.

Chapter 2

Nuclear Magnetic Resonance

Nuclear Magnetic Resonance (NMR) is a physical phenomenon in which the atomic nucleus interacts with an external magnetic field by absorbing and re-emitting electromagnetic radiation. In resonance, the external force transfers energy to the system at the resonant frequency of the system. In NMR, the resonance is produced by magnetic field oscillating at the resonant frequency of the studied nuclei. The resonant frequencies of the nuclei studied by NMR range from 10 to 800 MHz corresponding to radio frequencies of the spectrum of electromagnetic radiation. The advantage of using of radio frequency radiation are that the radiation is non-ionizing and it does not damage the sample.

This chapter introduces the basic principles of the NMR phenomenon and NMR experiments. The chapter is based on the lecture notes of the courses [5,12] of the University of Oulu and the book 'Understanding NMR spectroscopy' written by James Keeler [11].

2.1 Atomic nucleus in an external magnetic field

The understanding of quantum properties of a nucleus in a magnetic field is essential for understanding the NMR phenomenon. In this section, the response of an atomic nucleus to the external magnetic field is first introduced quantum mechanically and then from the view of classical physics.

2.1.1 Magnetic properties of a nucleus

Matter consists of atoms which are composed of subatomic particles of protons, electrons and neutrons. The nucleus of an atom is formed by positively charged protons and electrically neutral neutrons and the nucleus is surrounded by the negatively charged electron cloud. In terms of NMR phenomenon, the properties of an atomic nucleus are the subject of special interest.

The NMR phenomenon requires a nucleus possessing a quantum property called spin which is described with a spin quantum number I. Nuclear spin can be thought of as an intrinsic angular momentum analogous to classical internal angular momentum of a particle rotating around a spinning axis. Quantization is a physical phenomenon in which, instead of a continuous distribution, a physical quantity can possess only certain discrete values. The angular momentum vector of a particle can possess $2I+1$ different orientations in relative to the chosen direction. The possible values of I are characterized as $m = -I, -I+1, ..., I-1, I$. For example, protons and neutrons possess spin value $I = \frac{1}{2}$ which can orientate in two ways: either spin-up $m = +\frac{1}{2}$ or spin-down $m = -\frac{1}{2}$ state. If the number of protons and neutrons in a nucleus is even, the spins having opposite signs can pair up and eliminate each other giving zero total spin. Depending on a number of nucleons in an atom, the overall spin of a nucleus can possess half-integer values of 0, $\frac{1}{2}$, 1, $\frac{3}{2}$ etc. Only nuclei with non-zero overall spin are involved in the NMR phenomenon.

A nucleus possessing spin has an intrinsic spin angular momentum $\boldsymbol{J}$ magnitude of which can be defined as

$$J = |\boldsymbol{J}| = \hbar\sqrt{I(I+1)}, \tag{2.1}$$

where $\hbar$ is reduced Planck's constant ($\hbar = \frac{h}{2\pi}$) and I is a spin quantum number of a nucleus having half-integer values $I = 0, \frac{1}{2}, 1, \frac{3}{2}, ...$

Nucleus having a spin angular momentum is also associated with a magnetic dipole moment

$$\boldsymbol{\mu} = \gamma \boldsymbol{J}, \tag{2.2}$$

where γ is a nucleus-specific gyromagnetic ratio. Due to quantization of the spin angular momentum, the dipole moment is also quantized and its magnitude is

$$\mu = |\boldsymbol{\mu}| = \gamma\hbar\sqrt{I(I+1)}. \tag{2.3}$$

If a nucleus having a magnetic dipole moment is placed in an external magnetic field $\boldsymbol{B}$, the field interacts with a dipole moment by generating a torque $\boldsymbol{\tau} = \boldsymbol{\mu} \times \boldsymbol{B}$ and the axis of the dipole moment vector starts to rotate from its original position. The phenomenon is called precession or gyration movement (Figure 2.1). The rotational frequency around the direction of the external magnetic field is called Larmor frequency and it is defined by equation

$$\nu = \frac{\gamma}{2\pi} B_0 \tag{2.4}$$

or as an angular frequency

$$\omega = \gamma B_0. \tag{2.5}$$

In an external magnetic field, there are two possible energy states for spin-half nucleus defined as

$$E_m = -m\hbar\gamma B_0 \longrightarrow \begin{cases} E_\alpha = -\frac{1}{2}\hbar\gamma B_0 \\ E_\beta = \frac{1}{2}\hbar\gamma B_0 \end{cases}, \tag{2.6}$$

where the lower energy state is named as α and higher energy state as β. More generally, due to nature of quantum mechanics, the energy of a spin-half particle can be written as superposition of these two states.

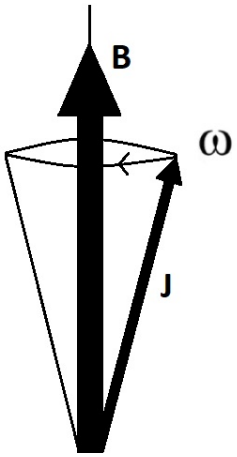

Figure 2.1: Illustration of Larmor precession.

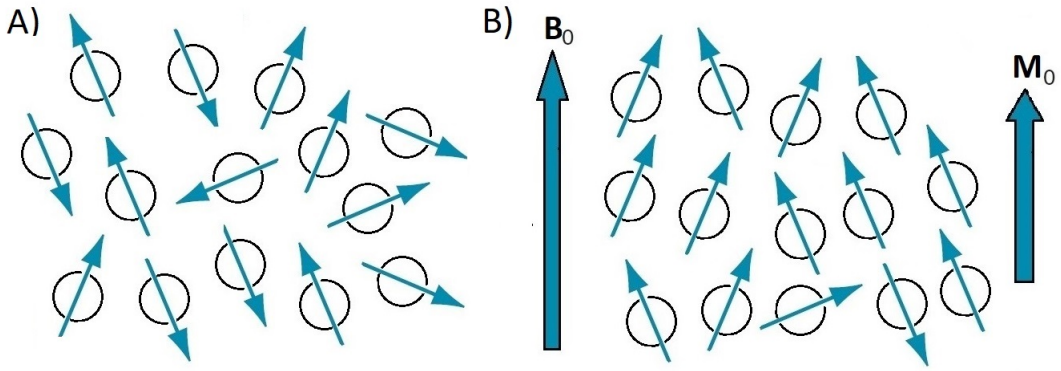

Figure 2.2: A) Without external magnetic field, spins are randomly orientated and the bulk magnetization summed over the spins is zero. B) In presence of external magnetic field, randomly oriented spins tend to align with the field and the bulk magnetization grows up.

2.1.2 The bulk magnetization

In NMR, instead of measuring individual nuclear magnetizations, it is more practical to study magnetization macroscopically. The overall magnetization of the studied nuclei can be represented by the bulk magnetization vector. The vector model makes the study of magnetization more convenient because the behaviour of the vector is completely classical and no quantum mechanics are needed.

The nuclei possessing a spin can be considered as a small magnets tending to turn parallel to the external magnetic field. When a nucleus having spin is placed in a magnetic field, the dipole moment of the nucleus interacts with the field. The energy of the interaction depends on the angle between the field and the dipole moment vector and it is minimized when the angle is zero. For that reason, the nuclei show a preferential orientation parallel to the field to minimize their energy. However, there is thermal motion in the system causing the magnetic moments to be randomly orientated. The overall bulk magnetization is the vector sum of all individual magnetic moments but despite the random orientations of magnetic moments, there is a slight net magnetization parallel to the external field. The observable magnetization is called the equilibrium magnetization M_0. The effect of adding external magnetic field on spin orientations and the bulk magnetization is illustrated in Figure 2.2.

Assuming that the nuclei are identical and the system is at thermal equilibrium,

summing up the magnetic moments of the nuclei gives the magnitude of the macroscopic magnetization M_0 parallel to external magnetic field B_0 as

$$M_0 = \frac{N\gamma^2\hbar^2 I(I+1)}{3kT} B_0, \tag{2.7}$$

where N is the number of nuclei, k Boltzmann's constant and T temperature in Kelvin. The term kT determines the effect of thermal energy; the higher the temperature, the smaller the bulk magnetization.

Based on Equation (2.7), the magnitude of the equilibrium magnetization is proportional to the gyromagnetic ratio which is characteristic to a nuclear isotope. A hydrogen nucleus or proton (^{1}H) possesses the largest gyromagnetic ratio of all stable nuclei. A proton is also the most commonly occurring nucleus in biological systems due to a water molecule (H_2O) including two hydrogen atoms. For these reasons, a proton is the most used nucleus in NMR spectroscopy. Other nuclei commonly probed by NMR are shown in Table 2.1 below.

Nucleus	**Overall spin**	**Natural abundance (%)**	γ ($\frac{\text{rad}}{\text{Ts}} \cdot 10^7$)
^{1}H	1/2	99.985	26.752
^{2}H	1	0.015	4.107
^{13}C	1/2	1.108	6.728
^{17}O	5/2	0.037	-3.628
^{14}N	1	99.630	1.934
^{19}F	1/2	100	25.181
^{23}Na	3/2	100	11.27
^{31}P	1/2	100	10.841
^{129}Xe	1/2	26.44	-7.452

Table 2.1: Properties of nuclear isotopes commonly used in NMR [5].

2.2 Basics of NMR experiment

A very basic NMR experiment consists of a radio frequency excitation pulse, relaxation and signal acquisition. The principles of the NMR experiment are introduced in this section.

2.2.1 RF excitation

At the beginning of an NMR experiment, a sample containing a set of non-zero spin nuclei is placed in strong, homogeneous, external magnetic field B_0 strength of which is usually several tesla. After a while, the equilibrium magnetization M_0 has built up and the behaviour of the magnetization can be described with this macroscopic magnetization vector. Assume that the equilibrium magnetization is aligned with positive z-axis at the beginning. Next, the much weaker radio frequency (RF) field B_1 oscillating at the frequency equal or close to Larmor frequency of the nuclei is applied along the xy-plane. The RF field applies a force to $\boldsymbol{M}$ and as a result, the magnetization vector $\boldsymbol{M}$ rotates towards the xy-plane. Viewed from the frame rotating around the z-axis at the Larmor frequency, during the pulse of length t, the $\boldsymbol{M}$ vector flips to the angle of

$$\theta = \gamma B_1 t \tag{2.8}$$

from the z-axis. This rotation of magnetization from its equilibrium is called an RF excitation.

The oscillating B_1 field is generated by a coil that produces an oscillating alternating current at the resonant frequency. The length of the B_1 pulse can be chosen arbitrary but most ofter in such a way that the magnetization vector forms 90^{o} or 180^{o} angle with the main magnetic field. After the RF pulse, the magnetization in the xy-plane precesses and induces alternating voltage, the magnitude of which is proportional to the magnitude of the transverse component of the magnetization through the coil around the sample. Due to a process called relaxation, after a finite time after the RF excitation, the magnetization returns to its equilibrium. Because the transverse magnetization decays during the signal acquisition, the NMR signal is called a free induction decay signal or FID (Figure 2.3). In order to improve the signal-to-noise ratio, the NMR experiment is usually repeated several times and the recorded FIDs are summed up.

2.2.2 Relaxation

During relaxation, the magnetization of the spins recovers to the equilibrium. The relaxation in NMR takes usually from milliseconds to seconds which is an especially long lifetime of an excited state compared to electronic or molecular excitation states lasting from nanoseconds to microseconds. The relatively slow relaxation has many advantages and makes it possible to manipulate and detect the magnetization. The

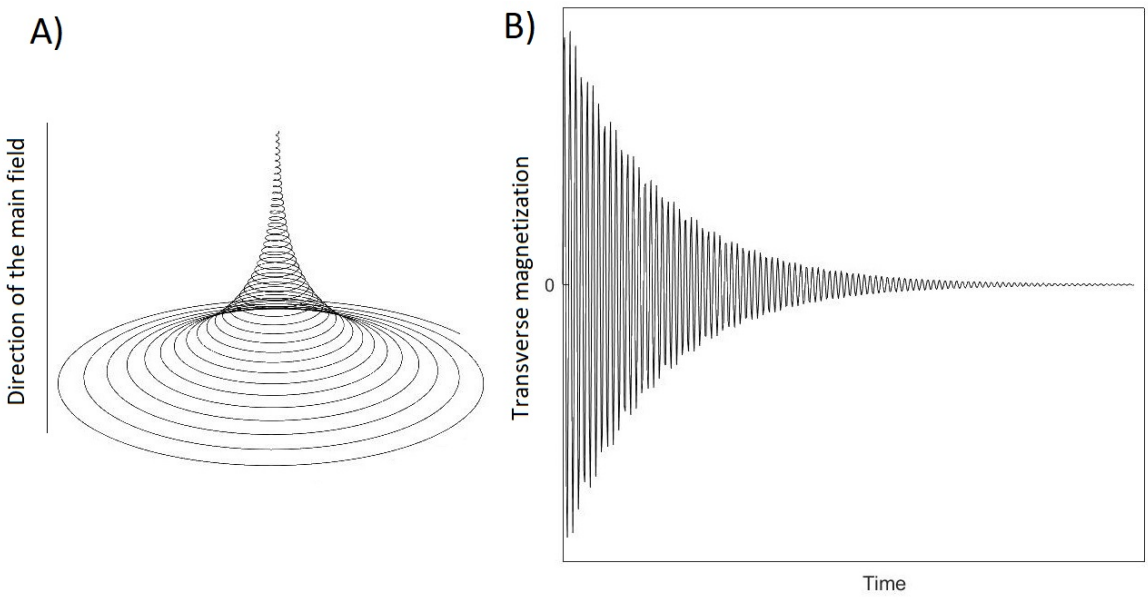

Figure 2.3: The free induction decay. A) An illustration of the movement of the tip of the magnetization vector in laboratory frame. B) FID signal representing the decay of transverse magnetization during relaxation.

relaxation in NMR is also very sensitive to the chemical and physical environment and the motion of the molecules which provides valuable information on the molecular surroundings and dynamics.

In NMR, the spins experience two types of relaxation, transverse relaxation which occurs in the xy-plane and longitudinal relaxation which describes the return to equilibrium with B_0. The longitudinal and transverse magnetization have their own relaxation times and therefore the NMR relaxation can be characterized using two relaxation processes called T_1 and T_2 relaxation. When the excited magnetic moment of spin rotates back towards the equilibrium, the energy received in excitation flows back to environment and for that reason T_1 relaxation is also called spin-lattice relaxation. T_2 relaxation describes the attenuation of the transverse magnetization to its equilibrium value zero but the occupations of energy levels do not change as in T_1 relaxation. T_2 relaxation time is always shorter or equal to T_1 relaxation time, in other words, the transverse magnetization decays faster than longitudinal magnetization recovers.

Relaxation mechanisms

The local fluctuating magnetic fields are the source of relaxation in NMR. Due to the naturally occurring heat movement of the molecules, the local fields rotating near the Larmor frequency can act as an RF pulse and change the orientations of the magnetic moments of the spins. The local fields can also add up with external magnetic field and change the precession frequencies of the spins. The sources of local magnetic fields are called relaxation mechanisms and, in case of spin-half nuclei, the most significant mechanisms are dipolar mechanism, chemical shift anisotropy and spin-rotation interaction.

In the dipolar mechanism, the local fields experienced by the spin arise from the magnetic dipole moments of other spins. The magnitude of the local field depends on the orientation of the spins in relation to the external field because the orientations of the spins do not change as the molecules rotate. As a result of molecular rotation, the spin experiences a fluctuating local field that gives rise to relaxation.

In presence of strong magnetic field, the field forces the electrons of an atom on circular motion around the direction of the field. Motion of negatively charged electrons around the positively charged nucleus generate electric currents which furthermore create small local magnetic fields around the nucleus. The magnetic field experienced by the nucleus is shielded by the smaller induced magnetic fields caused by the electrons and the precession frequency is now defined as

$$\nu = \frac{\gamma}{2\pi}(1-\sigma)B_0, \tag{2.9}$$

where σ is the shielding constant which depends on the electronic environment of the nucleus. The difference between precession frequencies of the nuclei located in different electronic environments is called chemical shift.

Chemical shift anisotropy describes how the size and direction of a shielding magnetic field depend on the orientation of the molecule with respect to the external field. As the molecules rotate, the local field vary and this variation in magnetic field is a source of relaxation. The magnetic fields generated by electron movement may also interact with magnetic moments of other nuclei which is called spin-rotation interaction. When the rotational frequencies of molecules change, for example as a result of molecular collisions, the local fields also change which causes relaxation.

T_1 relaxation

Before excitation, there is only equilibrium magnetization M_0 and no transverse magnetization. The RF pulse tilts the magnetization to an angle θ from z-axis causing the longitudinal component M_z to decrease and transverse component M_{xy} to increase accordingly. The growth of longitudinal magnetization back to the equilibrium can be described with the Bloch equation

$$\frac{d(M_z(t) - M_0)}{dt} = -\frac{M_z(t) - M_0}{T_1}. \tag{2.10}$$

The most commonly used method by which the T_1 relaxation time can be deduced is a pulse sequence called inversion recovery which is a simple experiment composed of two RF pulses (Figure 2.4 A). First, the equilibrium magnetization is rotated by a 180° pulse to the negative z-axis and it is given time to recover for a delay τ. Due to the fact that only transverse magnetization can be detected in NMR experiment, the magnetization is furthermore flipped to the xy-plane using a 90° pulse. Supposing that at time t = 0 $M_z(0) = -M_0$, the magnitude of M_z follows the equation

$$M_z(t) = M_0[1 - 2e^{-\frac{t}{T_1}}]. \tag{2.11}$$

The inversion recovery is repeated using varying delays of τ during which the magnitude of M_z grows from negative to zero and then to positive equilibrium value (Figure

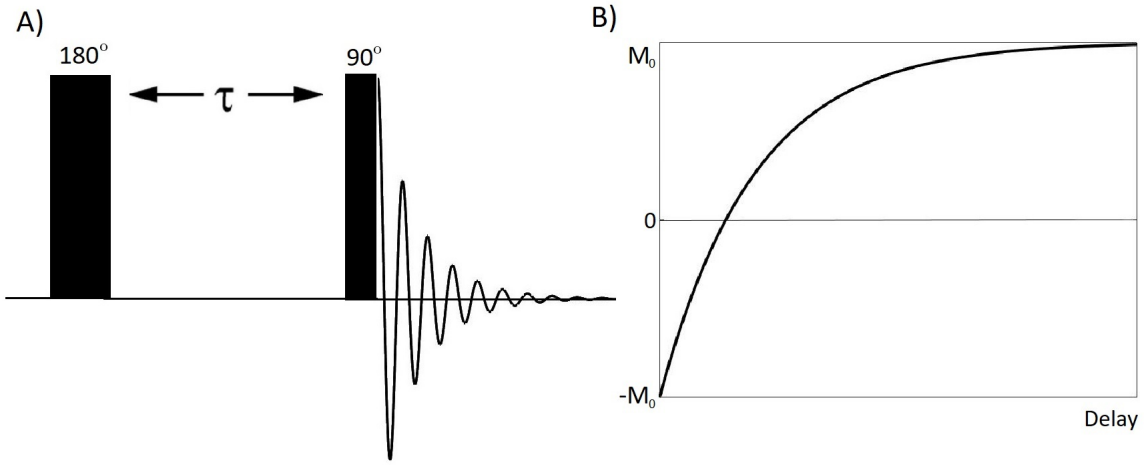

Figure 2.4: A) Inversion recovery pulse sequence. B) The signal growth in T_1 relaxation.

2.4 B). The T_1 relaxation time can be obtained by fitting the values of z-magnetization to the Equation (2.10).

T_2 relaxation

T_2 relaxation time depicts the decay of transverse magnetization back to its equilibrium value zero. The magnitude of transverse component of the magnetization obeys the Bloch equation

$$\frac{dM_{xy}(t)}{dt} = -\frac{M_{xy}(t)}{T_2}. \tag{2.12}$$

After rotating magnetization to the xy-plane, the decay of the transverse magnetization can be described with the equation

$$M_{xy}(t) = M_0 e^{-\frac{t}{T_2}}. \tag{2.13}$$

There are small inhomogeneities in external B_0 field and due to these inhomogeneities, magnetic moment vectors of spins in different locations are precessing with varying frequencies the making the magnetization vectors of individual spins to scatter. The bulk magnetization is a sum of individual magnetic moments and, due to that, the transverse magnetization decays more rapidly than only T_2 relaxation provides. This decay originating from B_0 inhomogeneities is described with relaxation time T_2^* (Figure 2.5 C).

The dephasing of magnetization vectors due to variations in B_0 inhomogeneities can be eliminated with the spin echo pulse sequence (Figure 2.5 A). In spin echo, the equilibrium magnetization is rotated to the negative y-axis by a 90° pulse. Due to variations in local Larmor frequencies, individual magnetization vectors are moving away from the negative y-axis with varying speeds and the magnitude of detectable magnetization decays. After dephasing for a delay τ, the magnetization is flipped to the positive y-axis by a 180° pulse. As a result, the magnetization vectors are now approaching each other and reuniting on the positive y-axis which forms an echo. T_2 relaxation time can be deduced by repeating the spin echo experiment with increasing delays and fitting the measured signal intensities to Equation (2.13).

Alternatively, in case of measuring dynamic processes of biological macromolecules, the Carr-Purcell-Meiboom-Gill (CPMG) pulse sequence is a more preferable method to determine T_2. In CPMG, there is a 90° pulse and after that, instead of a single

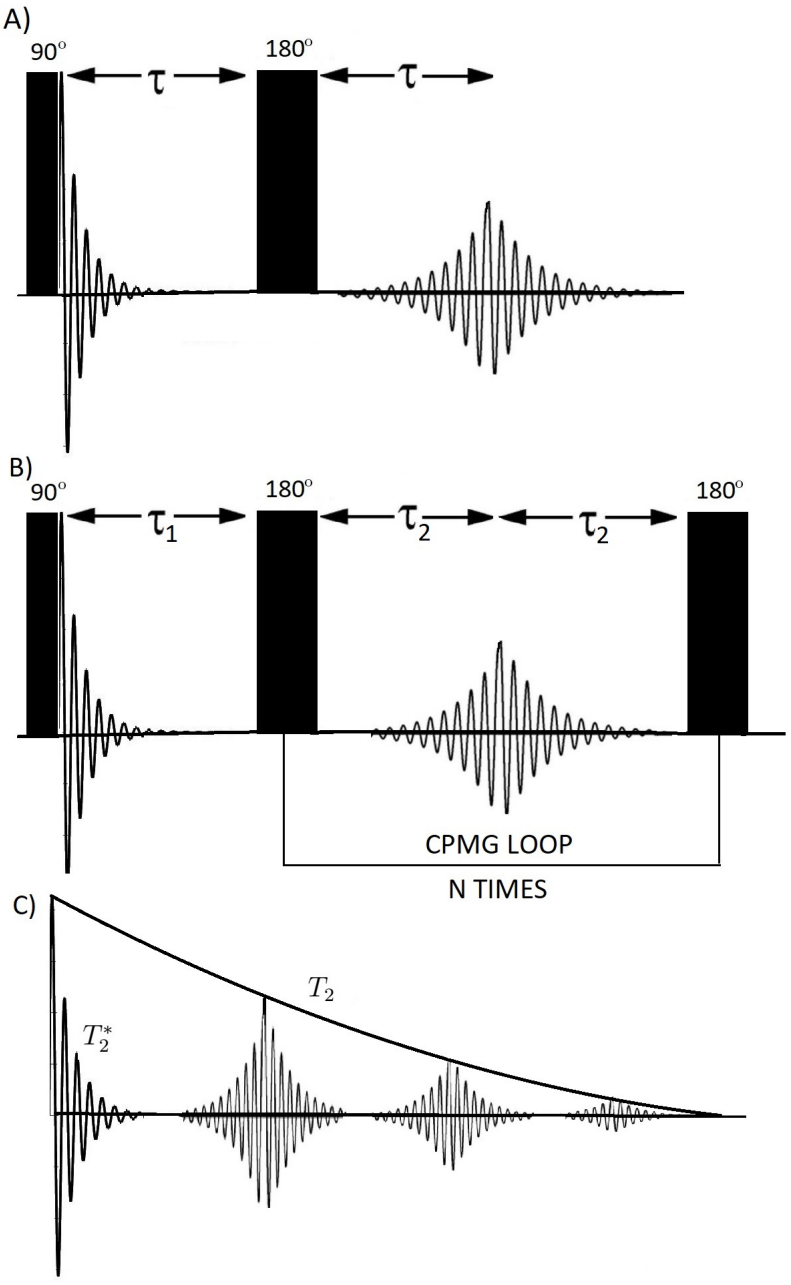

Figure 2.5: A) Spin echo pulse sequence. B) CPMG pulse sequence with N loops. C) Illustration of signal acquisition in CPMG.

180° pulse, there is a loop of 180° pulses. Compared to spin echo, there is a phase difference between a 90° and 180° pulses. The use of phase differences allows measurement of short time-scale exchange processes of biological systems. As the 180° pulse is repeated, as a result there is a train of echoes, the magnitude of which corresponds T_2 relaxation (Figure 2.5 B, C) [13].

Chapter 3

NMR Cryoporometry

Nuclear Magnetic Resonance Cryoporometry (NMRC) is one of a handful of thermoporometry methods used to acquire information on the pore size distributions of porous materials. Depending on the absorbed liquid, thermoporometry is suitable for determining pore diameters between 2 nm and 1 µm. In addition to characterizing the porosity of the material, NMRC can be paired with other NMR measurements to identify the liquid properties in porous materials, for example, diffusion and pore surface interactions. The method can be used to study a wide variety of materials such as gels, cement, rocks, wood or biological systems such as bone or skin [9,10,14].

One of the most widely used methods of thermoporometry is differential scanning calorimetry (DSC) which is based on the same principles as NMRC but it measures transient heat flow instead of NMR signal. NMRC and DSC have many advantages compared to other pore characterizing methods because they are non-destructive and the studied samples are able to be reused after experiments. The advantage of NMRC over DSC is that experiment can be performed arbitrarily slowly and there is no minimum rate for the measured signal. As a method, NMRC is simple and safe to carry out because there is no need for toxic chemicals or time-consuming sample preparation [9,10,14].

3.1 Theory

Thermoporometry is based on detecting the phase transition of a substance confined in porous material and naturally the understanding of thermodynamics is essential in case of the theory. Most commonly studied phase transitions in thermoporometry are from solid to liquid or vice versa [14]. This section concentrates on the theory related

to the phase transition from solid to liquid.

3.1.1 The Gibbs-Thomson equation

The transition from one phase to another can occur if the free energies of these states are equal [14]. In liquid confined in a small pore, the capillary effect and curvature of pore surface under tension decreases the melting-freezing point of confined liquid. The phenomenon is described by the Gibbs-Thomson equation whereby the shift in a melting-freezing point of the liquid is inversely proportional to the pore size. The Gibbs-Thomson equation defines depression of melting point of liquid in a spherical shaped pore as

$$\Delta T_m = T^0 - T_m = \frac{4\sigma_{sl}T^0}{H_f \rho_f a} = \frac{k}{a}, \tag{3.1}$$

where T^0 is the melting point of the bulk liquid, T_m melting point of the liquid confined in a pore, σ_{sl} solid-liquid interface energy, H_f bulk enthalpy of fusion, ρ_f density of solid and a the diameter of a pore. The equation can be simplified using the calibration constant k which takes into account the pore geometry and the properties of liquid and solid states of the absorbed substance and the interaction between these two states. The value of a constant k cannot be known in advance or derived but it can be evaluated by calibration experiments using samples with well known pore dimensions such as porous silica gels. However, usually real samples may have a mixture of different pore geometries and the choice of calibration constant is not entirely unambiguous [9]. The calibrated k-values can also be found from the literature and for example for cylindrical shaped pores filled with water, the estimated k-values range between 21-53 nmK [14].

The Gibbs-Thomson equation can be written in form

$$\Delta T_m = \frac{k}{a} = k\frac{dA}{dV}, \tag{3.2}$$

where the term dA/dV represents the curvature of the solid-liquid interface in a pore. For example, the curvature is determined as $1/a$ for cylindrical pores and $2/a$ for spherical pores where a is the diameter of a pore; the higher the curvature, the greater the melting point depression [15].

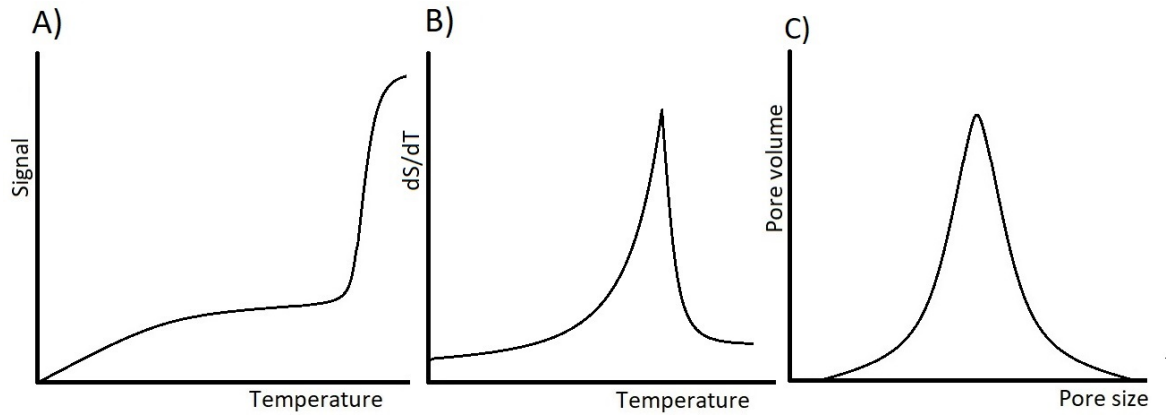

Figure 3.1: A) The melting curve is first transformed into B) dS/dT curve and finally into the C) pore size distribution.

3.1.2 Pore size distribution

In NMRC, the signal intensity of liquid water is measured as a function of temperature. The experiment results in a cryoporometric melting curve, the ideal form of which is shown in Figure 3.1. At the beginning of the melting, signal intensity is zero and there are no liquid state present in the sample. After that, there is a slow signal increase which corresponds to the melting of liquid in small pores and after that follows the total pore volume plateau. The steep increase of signal represents the melting of bulk liquid and at the end there is a total liquid volume plateau [9].

Because the signal intensity is directly proportional to the volume of the molten liquid, the pore size distribution can be derived from slope of the melting curve using the equation

$$p(r) = \frac{dV}{da} = \frac{k}{a^2}\frac{dS}{dT}, \tag{3.3}$$

where S is the signal of molten the liquid and T temperature [9].

Ideally, the magnetization of the sample does not depend on temperature but, according to the Curie's law, the magnetization of the sample is inversely proportional to temperature. This temperature dependence of magnetization and NMR signal intensity can be corrected by the equation

$$\frac{S(T_K)}{S(273\ \mathrm{K})} = \frac{273\ \mathrm{K}}{T_K},$$

where signal intensity S at temperature T_K is corrected in relation to the signal intensity at 273 K. However, in NMRC of liquids, the phenomenon is not very significant and can usually be ignored [9,14].

3.1.3 Layer of non-freezing liquid

In calculations of pore size distribution, it must be taken into account that there possibly exists a layer of non-freezing liquid between the pore wall and solid core. In small pores, the unfrozen layer can take up a significant volume of the total pore volume [9,10,14]. One explanation for the existence of such a non-freezing layer is based on the wetting theory which says that the free energy of liquid-solid interface is smaller than that of solid-solid interface. In other words, the system aims to thermodynamic equilibrium by forming a liquid layer between the two solid states [16]. The thickness of non-freezing layer depend on the absorbed liquid. For example for water, the most commonly suggested values range between 0.5-0.8 nm which corresponds to 1-3 monolayers of water [10,17].

Taking into account the layer of non-freezing liquid, the Gibbs-Thomson equation is

$$\Delta T_m = \frac{k}{a - \delta}, \tag{3.4}$$

where δ is the thickness of non-freezing layer [15,17].

3.1.4 Freezing-melting hysteresis

In liquids confined in porous materials, there occurs a phenomenon called freezing melting hysteresis which means that freezing occurs at a lower temperature than melting. Because hysteresis changes the melting behaviour of the liquid, it can affect also to the pore size distributions obtained from the melting curve data [18,19].

There are several theories explaining the hysteresis effects in pore-filling liquids. It has been suggested that the melting occurs at higher temperatures than freezing because the system is trapped in a metastable state having higher free energy than the state of thermodynamic equilibrium. The metastability of the solid state originates from the high surface to volume ratio i.e. the curvature of the pore. The melting of a liquid in a pore starts in core and propagates towards the pore wall. In order for a solid core to melt, it must exceed a energy barrier which is why the melting takes place at

a higher temperature where the energy barrier is lower [10,14,15,18,19].

Other theory is a pore blocking effect which says that if there is a larger pore isolated by a smaller pore and the freezing starts as a nucleation outside the pore, the larger pore will freeze only after the temperature is low enough for the smaller pore to freeze. Also, it has been simply assumed that the freezing occurs in a lower temperature because there is a natural delay in propagation of nucleation. However, the freezing melting hysteresis can be problematic in case of determining the accurate pore size distributions but it can also be used to provide information on melting and freezing processes, pore connectivity and pore shapes in the porous materials [10,14,15,18,19].

3.2 NMRC experiment

In a cryoporometric experiment, one of the most commonly used liquid imbibed to porous material is water. Water is a good choice because it occurs often naturally in biological materials and ^{1}H provides strong NMR signal [9].

NMR is very useful tool for detecting phase transitions from solid to liquid because there is usually a considerable difference in T_2 relaxation times between liquid and solid states. In solids, T_2 is usually on the order of microseconds and in liquids from milliseconds to seconds. For that reason, the signals from solid and liquid can be distinguished by using the spin echo type pulse sequence as a T_2 filter. If the relaxation delay of the pulse sequence is set to be longer than the T_2 of solid but shorter than T_2 of liquid, the experiment results in a signal originating only from liquid state substance [9,14].

In an NMRC experiment, the sample is prepared such that the liquid fills the pores and to ensure liquid absorption the sample can be gently heated or centrifuged. After sample preparation, the sample is placed in NMR spectrometer and cooled down until the pore filling liquid is completely frozen. Then the sample is started to heat back to the starting temperature in small temperature steps while recording the signal. After each temperature step, there must be a long enough delay to ensure the system to reach thermal equilibrium. The signal acquisition as a function of temperature results in a cryoporometric melting curve (Figure 3.1) from which the pore size distribution can be derived [9,14].

Chapter 4

Articular Cartilage

Articular cartilage is an essential part of a synovial joint providing low-friction movement between two bones. The very specialized and unique structure of articular cartilage allows heavy loads to be carried but unfortunately in case of damage, the ability of the cartilage tissue to regenerate is very limited. The understanding of function and maintenance of articular cartilage is important to prevent, diagnose and heal joint diseases, the most common of which is the osteoarthritis causing pain and disability for millions of people [1,2,7,20].

4.1 Synovial joint

A joint is a place where two or more bones meet. The joints of human body can be classified into three types depending on whether the bones are directly or indirectly connected to each other: in fibrous and cartilaginous joints, the bones are directly connected by a connective tissue, and in synovial joint, the bones are indirectly connected by synovial cavity filled with lubricating fluid [20].

The synovial joint is the most common type of joint in a human body. The basic features of the synovial joint is shown in Figure 4.1. The synovial joint is surrounded by an articular capsule which encloses the joint cavity. The inner wall of articular capsule is covered by synovial membrane which produces the synovial fluid filling the joint cavity. At the end of the bone, there is a thin layer of articular cartilage reducing friction between the bones. In addition to synovial capsule, there are ligaments supporting the joint and tendons attaching the bones to muscles [20].

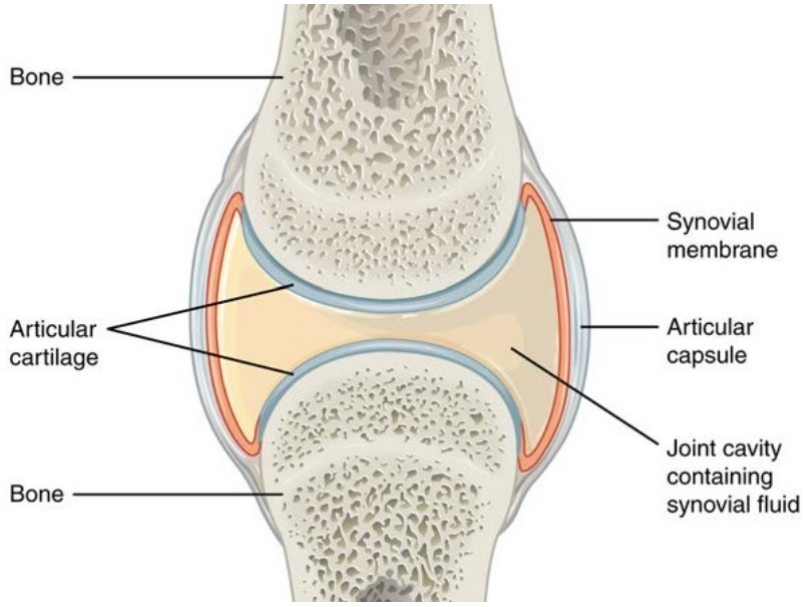

Figure 4.1: Anatomy of a synovial joint. *Anatomy and Physiology. OpenStax, 2013* [20].

4.2 Structure of articular cartilage

Articular cartilage is 0.5-5 mm thick layer of connective tissue covering the end of the bones [4]. The function of articular cartilage is to provide a low-friction gliding surface between the bones and to minimize peak pressures on the subchondral bone. Articular cartilage is a specialized tissue type of hyaline cartilage: it is white, glass-like, dense tissue lacking of nerves, blood vessels and lymphatics [1,4,7].

4.2.1 Components

The main components of articular cartilage are water, extracellular matrix of collagens and proteoglycans, and cartilage cells.

Collagens are proteins that make up approximately 10-20 % of the wet weight of articular cartilage. About 90 % of the collagen in articular cartilage is the type II collagen but there are also small amounts of other types of collagen helping to maintain the network of type II collagen. The main purpose of collagen in articular cartilage is to provide tensile strength to cartilage [1,4,7]. The diameter of individual type II collagen fibre is estimated to be 20-200 nm [4].

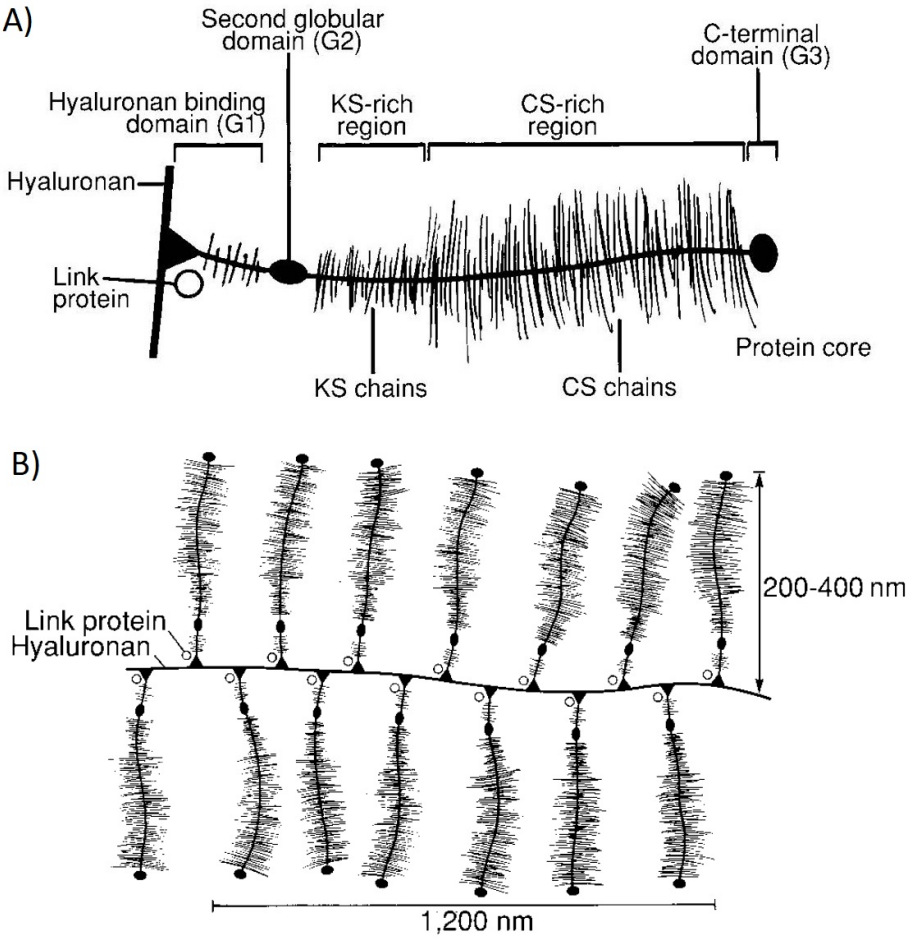

Figure 4.2: A) The aggrecan molecule. B) Proteoglycan aggrecate. *Restoration of Injured or Degenerated Articular Cartilage. Buckwalter et al, 1994* [25].

Proteoglycans are proteins forming 10-20 % of the wet weight of articular cartilage [7]. The subunits of proteoglycans are called glycosamino glycans (GAGs), the main types of which in cartilage are chondroitin sulphate (CS) and keratin sulphate (KS). GAGs can unite to a protein core and form large aggrecan molecules consisting of more than one hundred chondroitin and keratin sulfate chains (Figure 4.2 A). Due to the charge repulsion, the sulfate chains are extended out from the protein core and each other [1,4,7,21]. Furthermore, aggrecans can combine with hyaluronan via link proteins and form even more massive proteoglycan aggregates having approximated length of 2 µm (Figure 4.2 B) [21]. In addition to massive aggrecans, there are also smaller proteoglygans of decorin, biglycan and fibromodulin having similar protein structure but different GAG composition and function. Because of negative charge

of GAGs, they attract positively charged ions such as sodium and calcium causing the Donnan osmotic pressure. The osmotic properties of proteoglycans give cartilage its compressive strength and ability to swell and gain water [1,4,7,21]. Proteoglycans and collagen fibrils together form a water-filled porous network having estimated pore diameter between 2 and 6 nm [4].

Normal articular cartilage contains 65-80 weight percent water [1,7]. The frictional resistance and pressurization of water provide articular cartilage its ability to withstand significantly large loads [1]. Also, water provides lubrication and enables the transport and removal of nutrients and ions by diffusion [1,7,21]. A very small percentage of cartilage water is intracellular. Most of the interstitial water is free to move by diffusion but part of the water is bound in a porous network of collagen and proteoglycans [1,4,8].

Chondrocytes are the cells of hyaline cartilage covering only 1-5 % of the total volume of articular cartilage [7]. In articular cartilage, chondrocytes are spheroidal in shape and have the diameter of approximately 10 µm [22]. Chondrocytes are responsible for maintaining the cartilage metabolism by producing degradative enzymes. Chondrocytes also regenerate the matrix by synthesizing proteoglycans, collagens and noncollagenous proteins. In case of injury, chondrocytes have a low ability to regenerate themselves and the extracellular matrix which is a major factor in progressive cartilage degradation [1,7].

4.2.2 Ultra-structure

The ultra-structure of normal articular cartilage is represented in Figure 4.3 from which four different zones can be identified: the superficial zone, middle zone, deep zone and calcified zone.

The thin superficial zone is located just below the articular surface. In this zone, the chondrocytes are tightly packed and flat. The collagen fibres are packed tightly and aligned parallel to the articular surface. The dense, parallel alignment provides tensile and shear strength and protects the deeper layers of cartilage. The concentration of proteoglycans is low in this zone. The middle zone takes up to 60 % of the total cartilage volume and in this zone, the chondrocytes are spherical and sparsely spread, the concentration of proteoglycans is higher than in the superficial zone and

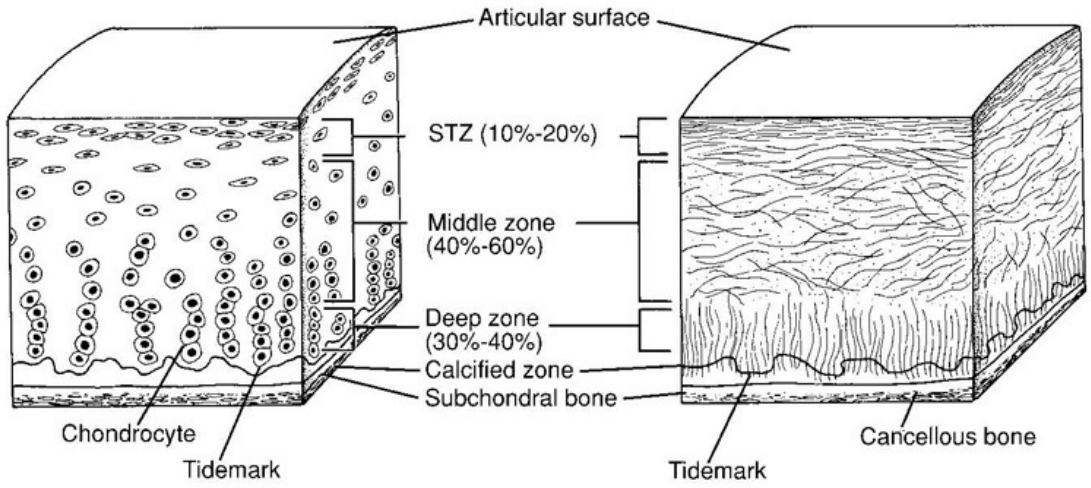

Figure 4.3: The ultra-structure of articular cartilage. On left, there is an illustration of chondrocyte organization and on right, alignment of collagen fibrils in the superficial tangential zone (STZ), middle zone and deep zone. *Restoration of Injured or Degenerated Articular Cartilage. Buckwalter et al, 1994* [25].

the collagen fibres have arbitrary orientations. The middle zone provides the first line compressive strength to cartilage. In the deep zone, the proteoglycan concentration is the highest and the collagen fibres and chondrocytes are aligned perpendicular to the articular surface which provides the highest compressive strength to the cartilage. The proportion of deep zone is 30-40 % of cartilage volume. The water concentration decreases from 80 % to 65 % from the superficial to the deep zone due to the increasing proteoglycan concentration. Below the deep zone, the calcified zone attaches the cartilage to the bone and there is only a small amount of hypertrophic i.e. enlarged chondrocytes. Between the deep and calcified zones, there is a visible 'tidemark' distinguishing the interface between the bone and cartilage [1,4,7,21,23].

4.3 Osteoarthritis

Osteoarthritis is a disease of progressive cartilage degeneration. Osteoarthritis may occur in any synovial joint but most commonly it occurs in a hand, hip or knee [24].

The progressive degeneration of articular cartilage is fundamentally due to the poor ability of the cartilage to regenerate after traumatic injury. Increasing age, trauma, obesity, genetic predisposition, hormonal and metabolic diseases and some inflamma-

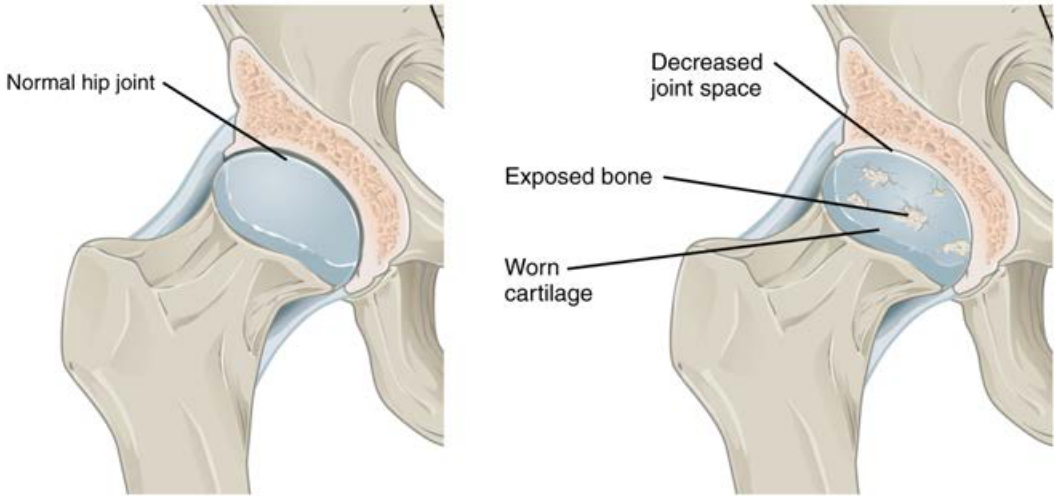

Figure 4.4: Comparison between a healthy joint and a joint with osteoarthritis. *Anatomy and Physiology. OpenStax, 2013* [20].

tions are the risk factors of degradation of articular cartilage [23].

The chondrocytes maintain and repair the cartilage matrix by forming and degrading tissue components. If tissue maintenance is disrupted and tissue degradation exceeds its formation, progressive cartilage degeneration occurs which can lead to osteoarthritis. As the osteoarthritis progresses, the length of proteoglycan chains gets shorter and the collagen fibres become disorganized which weakens the matrix. Due to the loss of proteoglycans, the pore size distribution of matrix increases and consequently the water concentration due to the higher permeability. In osteoarthritis, the water content may become over 90 % of the total tissue volume which reduces furthermore the load-bearing capacity of the matrix [1,4,7,21,25].

During degradation, the surface layer or cartilage wears off which causes friction during the joint movement. The loss of cartilage narrows the joint space whereupon the synovial membrane produces more synovial fluid causing the joint to swell. At the end-stage disease, the cartilage loss is so significant that the exposed ends of the bones rub against each other causing pain, stiffness, swelling and inability to move [12,23-25]. The comparison between healthy joint and osteoarthritis is shown in Figure 4.4.

Chapter 5

Brine and Phosphate-Buffered Saline

Brine or salt water is a solution of water and sodium chloride commonly known as table salt. The mixture of 9 $\frac{g}{L}$ NaCl and water is called saline. Sodium chloride plays a vital role in biological systems especially by maintaining fluid balance [20].

Phosphate-buffered saline (PBS) is buffer solution containing 8 $\frac{g}{L}$ sodium chloride, 200 $\frac{mg}{L}$ potassium chloride, 1.44 $\frac{g}{L}$ disodium hydrogen phosphate and 245 $\frac{mg}{L}$ potassium dihydrogen phosphate dissolved in water. In biological research, PBS in used to mimic the pH, ion concentrations and osmolarity of a human body [26]. The salt solution also prevents tissues swelling [8,20].

5.1 Eutectic phase transition

Eutectic is a combination of two or more components having lower freezing and melting points than any of its components. The freezing and melting of eutectics are a phenomenona called eutectic phase transitions [27]. Eutectic phase transitions has been observed in both saline and PBS [8,28,29].

The phase transitions of sodium chloride and water can be understood using the phase diagram of water with dissolved sodium chloride represented in Figure 5.1. From the diagram, it can be seen that the phase is dependent on the temperature and sodium chloride concentration. For the concentrations used in saline, a red line is marked in the figure.

As ice formation progresses and the amount of liquid water decreases, the salt concentration in the remaining brine increases and the melting point approaches the point

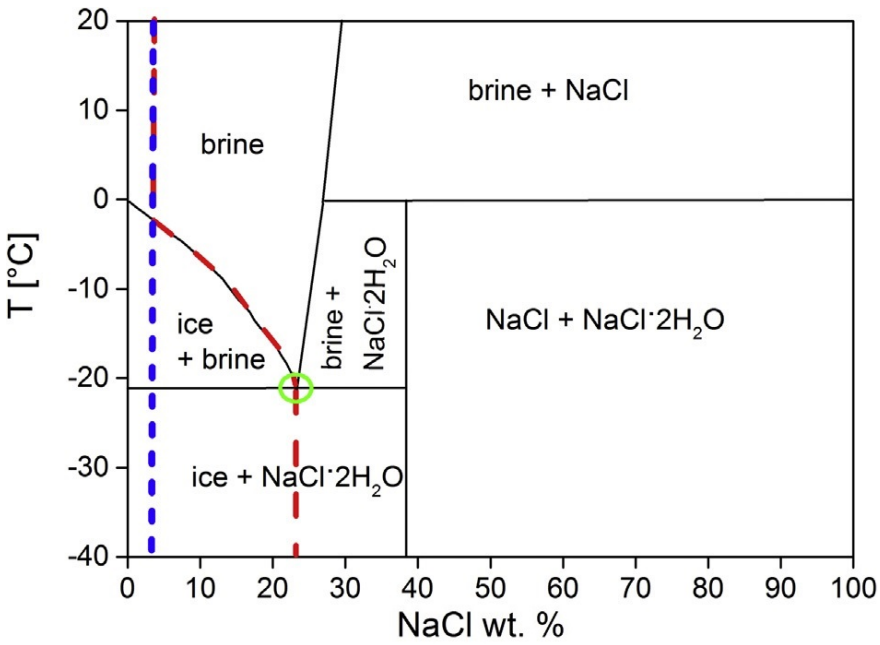

Figure 5.1: A phase diagram of water and sodium chloride solution. *New approach for determining cartilage pore size distribution: NaCl-thermoporometry. Majda et al. 2017* [8].

marked with the green circle. This point is called the eutectic point which occurs at the eutectic temperature below which the remaining brine solidifies into a hydrohalite crystals ($NaClH_2O$) [8,28-30].

From a cryoporometric point of view, it is essential to take into account eutectic phase transition when using salt solution as a solvent. The Gibbs-Thomson equation assumes that there is only one bulk melting point and the lower melting points are associated with liquid melting in pores. In case of salt solution, the hydrohalite melting causes an additional melting signal in cryoporometric melting curve which may obscure the signal associated with water melting in pores. The use of salt solutions as solvents in thermoporometry has not been studied systematically and the parameters used for cryoporometry calculations are not found in previous reports.

Chapter 6

Cryoporometric Experiments

In experimental part of this thesis, the ^{1}H NMR cryoporometry was performed to study phase transitions in porous materials with the end goal of quantifying the pore size distributions and measuring the associated T_2 relaxation in protein gels modelling the protein composition of articular cartilage. First, the phase transition of saline and PBS were studied and porous silica beads imbibed with water or saline were studied as controls. Lastly, the experiments were carried out with porous protein gels having varying protein concentrations. The purpose of the saline and silica bead controls is to better understand and characterize the melting behavior of saline in the prescence of a porous media. This is then applied for interpreting the data of protein gel experiments.

In the case of protein gels, the subject of the study was to measure pore size distributions of protein-associated water and T_2 relaxation in relation to protein content. In addition to measure pore size of cartilage, the purpose of the study was to identify which protein components water is associated with in articular cartilage.

Pore size and water concentration of articular cartilage are essentially related to compressive strength, joint health and osteoarthritis. The knowledge of pore size and water components of articular cartilage can help to understand the function, structure and different conditions of cartilage degradation. In many studies, T_2 relaxation linked to a range of disease markers including protein content and collagen alignment. The measurements of T_2 of articular cartilage may provide diagnosis of arthritis at early disease stages when cartilage extracellular matrix might be still reversible [31-33].

Figure 6.1: Bruker 500 MHz NMR spectrometer. The cooling system including liquid nitrogen tank and evaporator (on right) are connected connected to probe with a tube.

6.1 Hardware

The ^{1}H NMRC experiments were carried out using Bruker 500 MHz NMR spectrometer and 10 mm BBO probe (*Bruker, Karlsruhe, Germany*). The freezing was performed with liquid nitrogen evaporator. The spectrometer and cooling system are shown in Figure 6.1.

6.2 Saline and phosphate-buffered saline

In the first part of the experiment, the phase transitions of 9 $\frac{g}{L}$ saline and phosphate-buffered saline were studied. The study of the melting behaviour of saline solutions provides experimental understanding that helps in the next parts of the study with more complex samples. The hypothesis is that at 252 K, there occurs a eutectic phase transition which produces a peak in a PSD calculation [8].

6.2.1 Cryoporometry set-up

The samples were cooled from room temperature to 185 K for 2 hours to ensure the sample came to equilibrium. For saline sample, the temperature range was set from 185 K to 293 K by 1.15 K steps with total of 95 steps. The settling delay was 5 min/scan and 5 min/K for CPMG pulse sequence with 0.1 K accuracy. In CPMG, the echo time was 100 µs, number of echoes 5000, number of scans 64, recovery delay 3.5 seconds and experiment time 3 minutes. For PBS sample, the temperature range was set from 180 K to 280 K by 1.8 K steps with total of 58 steps. The settling delay was 5 min/scan and 10 min/K for CPMG with 0.1 K accuracy. In CPMG, the echo time was 500 µs, number of echoes 5000, number of scans 4, recovery delay 10 seconds and experiment time 3 minutes. The total experiment time was 18 hours.

6.2.2 Melting of saline and PBS

Melting curves of saline of PBS are shown in Figure 6.2 A. In order to detect phase transitions more clearly, the melting curves are converted to dS/dT curves shown in Figure 6.2 B. From these graphs it can be observed that there occur two separate phase transition in both samples during melting. Saline samples shows eutectic transition between 242-248 K and PBS between 242-250 K (marked with arrows). Both samples show continuous melting until bulk melting peak at around 270 K. Bulk melting shows wide distribution and starts at 257 K in both samples.

6.2.3 Pore size distributions

The pore size distributions were computed using parameters $T_0 = 273.15$ K and k=96 nmK [8] (spherical pore). The PSD graphs are represented in Figure 6.3 which shows sharp peaks of 4 nm and wide pore size distribution of 4-50 nm.

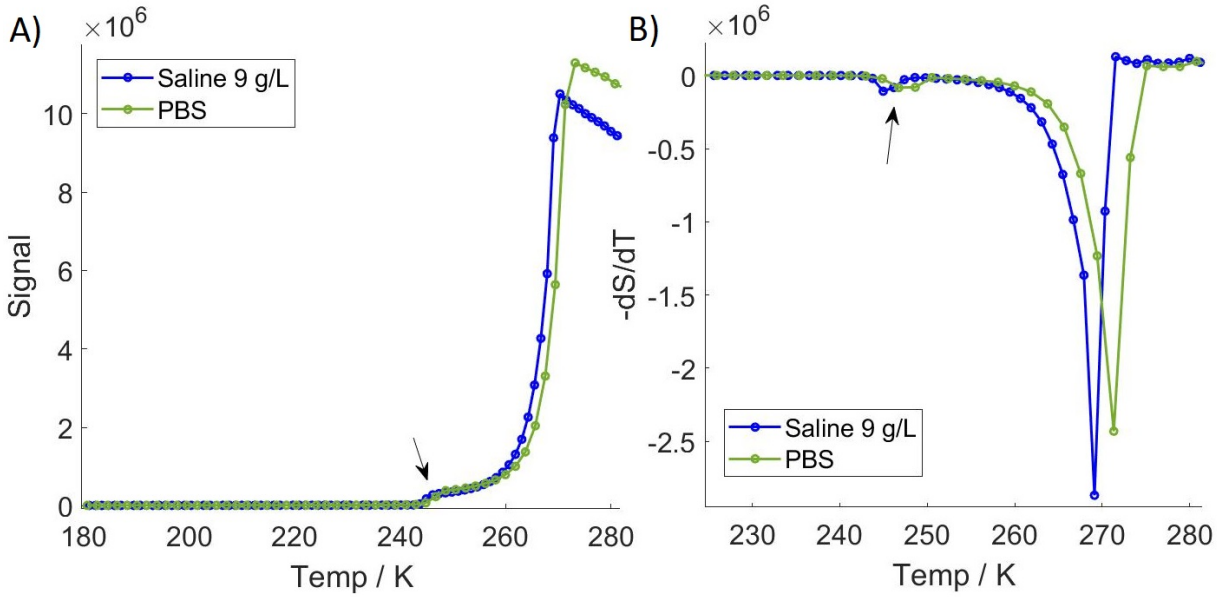

Figure 6.2: A) Melting curves and B) dS/dT curves of saline and PBS.

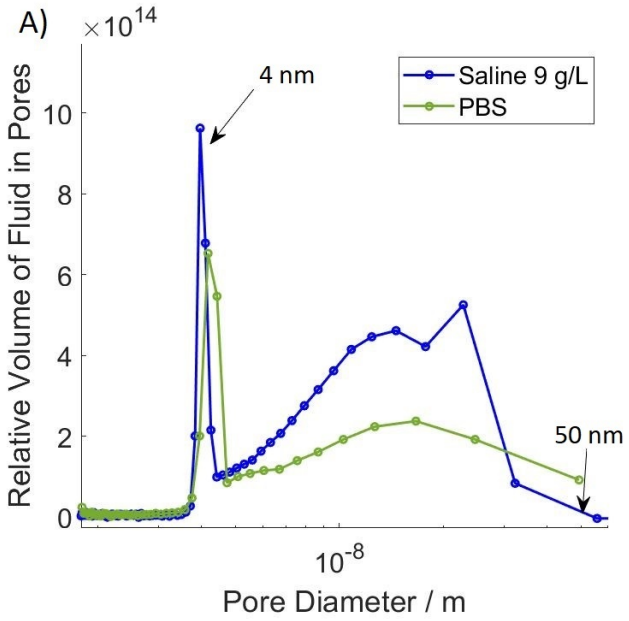

Figure 6.3: Pore size distribution of saline and PBS using $T_0 = 273.15$ K.

6.3 Silica controls

In the second part of the experiments, NMR cryoporometry was carried out with porous silica beads. The purpose of this part was to test the ability of the used cryoporometry set-up to distinguish between different pore sizes and to study how the porous material affects the melting behaviour of confined water or saline. In addition, the effect of changing T_0 parameter was studied. The hypothesis is that changing the value of T_0 below the eutectic temperature removes the eutectic peak from PSD, but also reduces the melting data to a few percent of total melting data which may also remove part of the essential pore-related data.

6.3.1 Samples

Samples of synthetic silica beads with a particle size of 200 µm and the inner pore diameter of 4 nm, 6 nm and 10 nm were prepared by placing the beads in 5 mm NMR tubes and then filling the bead packs with water or saline. A layer of free liquid was left on top of the bead pack to ensure the melting of bulk liquid as a reference (Figure 6.4). After that, the samples were heated in the oven at 333 K overnight to remove the air bubbles from the beads and to make silica bead packing uniform.

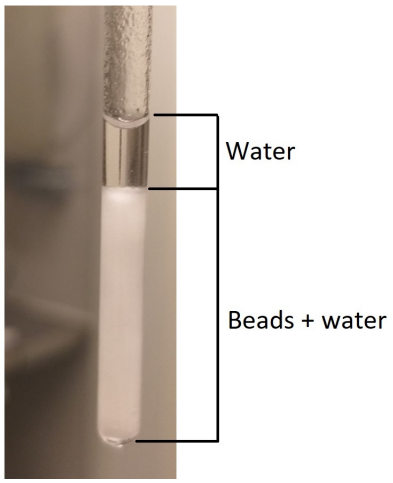

Figure 6.4: A sample of silica beads imbibed with water placed in a 5 mm NMR tube.

6.3.2 Cryoporometry set-up

The samples were cooled from room temperature to 185 K for 2 hours to ensure the sample came to equilibrium. The temperature range was set from 185 K to 293 K by

1.15 K steps with total of 95 steps. The settling delay was 5 min/scan and 5 min/K for CPMG pulse sequence with 0.1 K accuracy. In CPMG, the echo time was 100 µs, number of echoes 5000, number of scans 64, recovery delay 3.5 seconds and experiment time 3 minutes. The total experiment time including all steps was 18 hours.

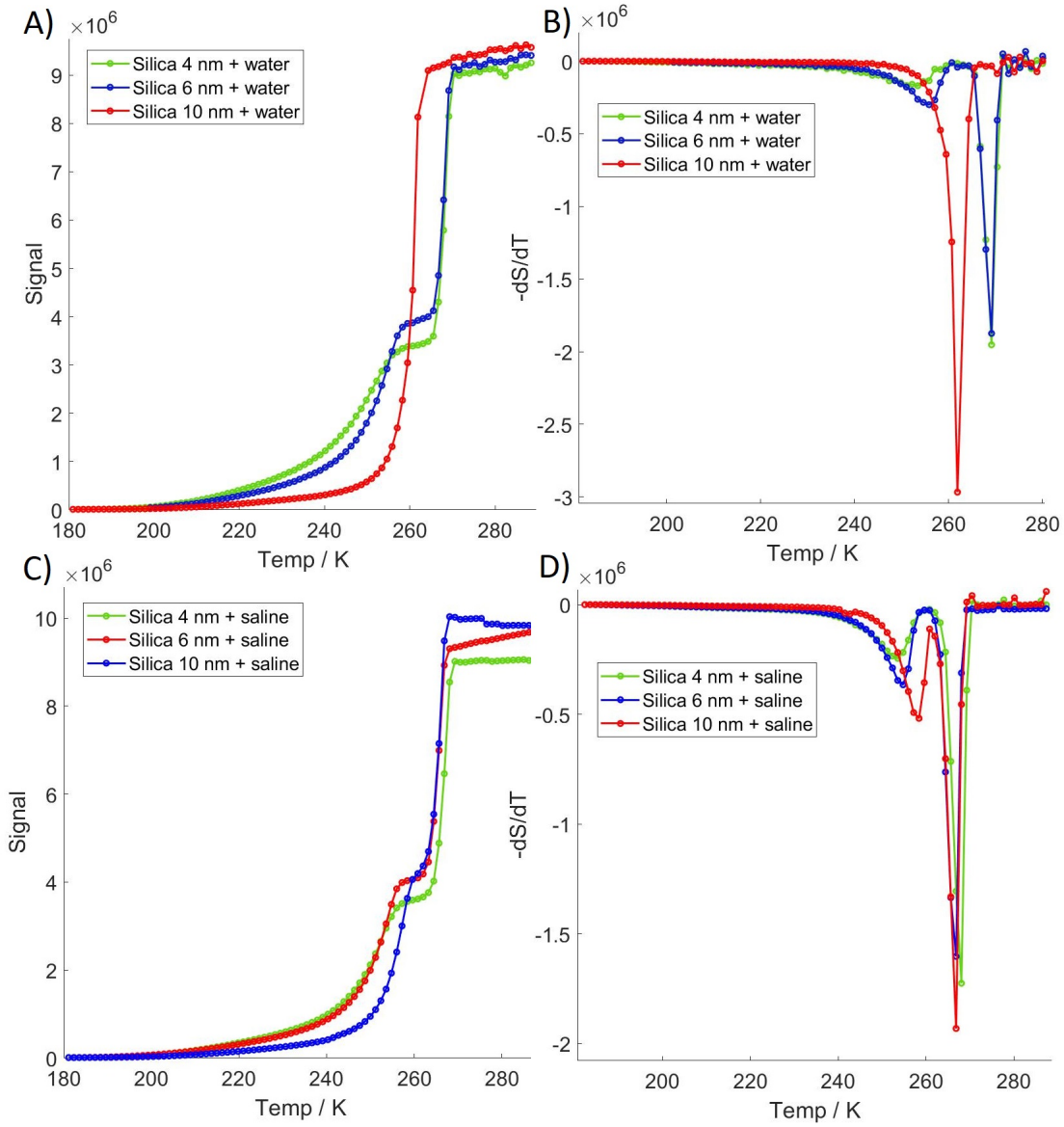

Figure 6.5: Melting curves and dS/dT curves of A,B) silica and water and C,D) silica and saline.

6.3.3 Water and saline melting in silica

The melting graphs of silica samples as a function of temperature are represented in Figure 6.5. The melting of water and saline seem to behave somewhat in the same way. It can be seen that the signal increase is very slow at low temperatures and at about 220 K signal starts to increase faster until 255 K. In saline, the bulk melting occurs at lower temperatures than in water. In water, the bulk water melting occurs between 264-272 K and in saline between 262-269 K. The pore-related signal increase occurs between 240-260 K which slightly depends on the sample. The 10 nm water sample behaves exceptionally showing only one steep increase of signal and bulk melting at 262 K. Both pore-related and bulk melting occur at a wide temperature range instead of one specific temperature. Clear signal increase of eutectic phase transition cannot be seen and it is likely to occur over a wide range as noted earlier.

6.3.4 Pore size distributions

The pore size distributions were computed using parameters $T_0 = 273.15$ K (Figure 6.6 A,B), $T_0 = 246$ K (Figure 6.6 C,D), k = 96 nmK [8] (spherical pore) and $\delta = 0.8$ nm [10].

Using $T_0 = 273.15$ K, all three water samples show a peak close to the corresponding pore diameter and smaller additional peaks at 2.5 nm. Samples of 4 nm and 6 nm show lower peaks at 20 nm. Saline samples show three peaks of 5 nm, 6 nm and 7 nm corresponding to samples of 4 nm, 6 nm and 10 nm. In saline samples, there are also additional peaks at 2.5 nm and 13-16 nm. 10 nm saline sample shows a tiny peak at 3.3 nm and 4 nm sample a shoulder at 4 nm which are very likely peaks of eutectic transition.

Using $T_0 = 246$ K, all samples show peaks at 3.5 nm which correspond to the smaller additional peaks observed above. It can be seen that decreasing the bulk melting point cuts major part of the peaks off and shifts diameters of remaining peaks to larger diameter area.

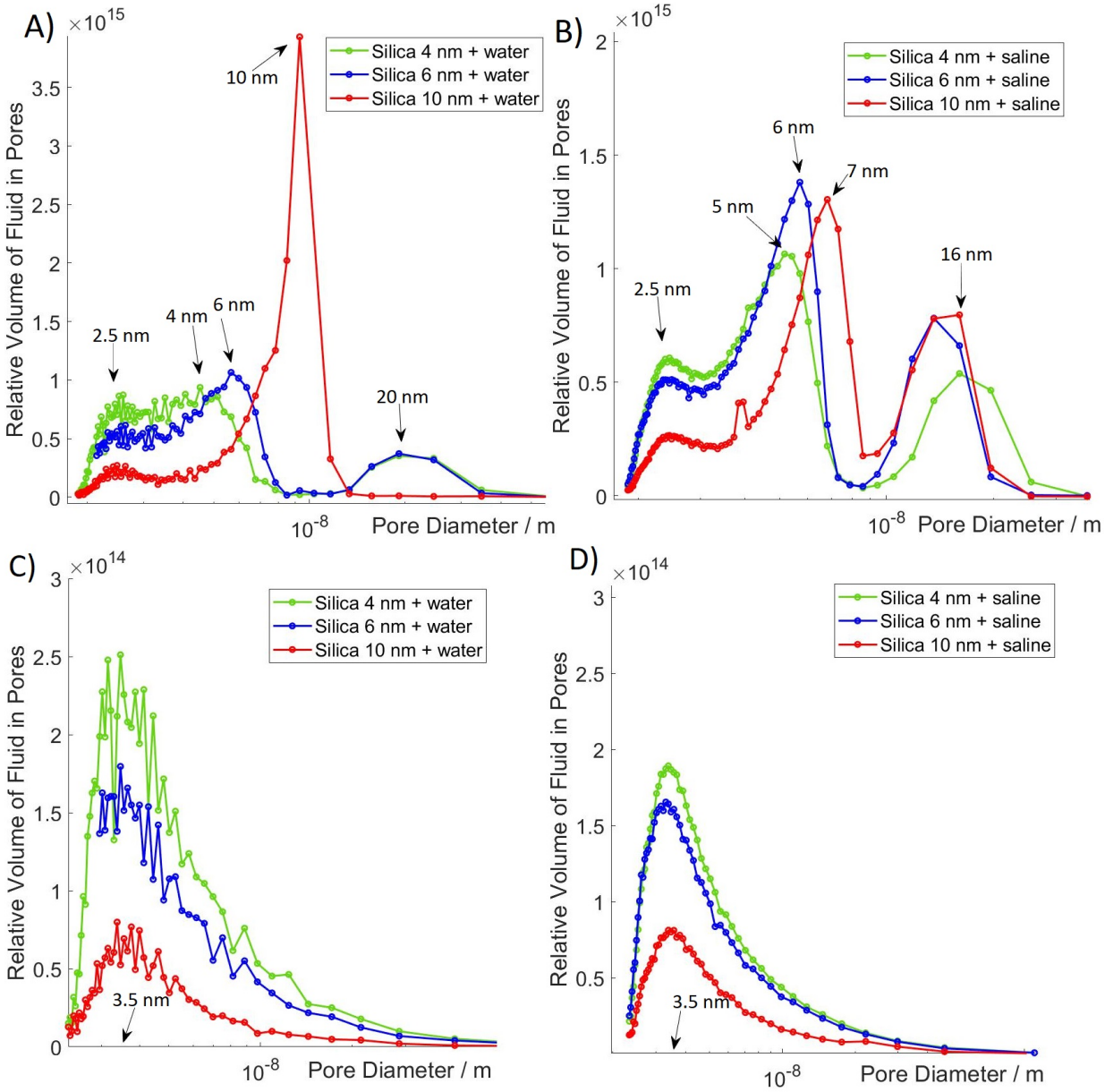

Figure 6.6: PSDs of silica controls using A,B) $T_0 = 273.15$ K and C,D) $T_0 = 246$ K.

6.4 Articular cartilage models

In the third part of the experiments, the protein hydrogels were used as a very simplified models of the extracellular matrix of articular cartilage. The total of 16 samples with different chondroitin sulfate and collagen concentrations were used to study the effect of varying protein concentrations on pore size distribution and T_2 relaxation. The main research questions are how articular cartilage tissue retains water, is the water associated with collagen fibres or chondroitin sulfates and whether it is possible to identify peaks associated with a particular protein, what is the effect of PBS as a solution, and is the T_2 relaxation time dependent on cartilage protein content especially at room temperature.

↓ Collagen | CS→	0 mg/g	5 mg/g	10 mg/g	20 mg/g
0 mg/g				
10 mg/g				
20 mg/g				
40 mg/g				

Figure 6.7: Collagen and chondroitin sulfate concentrations of used protein gels.

6.4.1 Samples

The protein hydrogels with collagen I concentrations of 0-40 $\frac{\text{mg}}{\text{g}}$ and CS concentrations of 0-20 $\frac{\text{mg}}{\text{g}}$ were used as models of cartilage matrix. The used combinations are represented in Figure 6.7. To keep the pH of the samples close to the pH = 7.4, PBS was used as a solution. The samples were stored in 253.15 K freezer before the experiments.

6.4.2 Cryoporometry set-up

The samples were cooled from room temperature to 185 K for 2 hours to ensure the sample came to equilibrium. The temperature range was set from 180 K to 280 K by 1.8 K steps. The settling delay was 5 min/scan and 10 min/K for CPMG with 0.1 K accuracy. In CPMG, the echo time was 500 µs, number of echoes 5000, number of scans, recovery delay 10 seconds and experiment time 3 minutes. The total experiment time including all temperature steps was 18 hours.

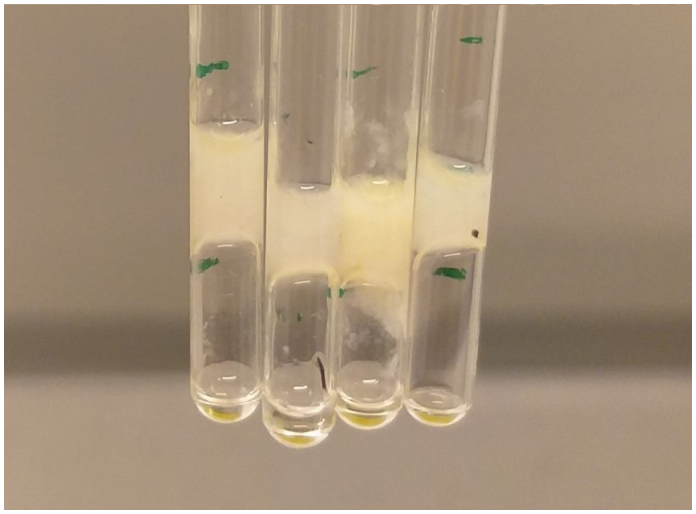

Figure 6.8: Four protein gel samples in 5 mm NMR tubes.

6.4.3 Effect of protein content on pore size distributions

In order to study whether water is associated with collagen or CS, first the amount of collagen was kept constant and concentration of CS was increased and vice versa. When the amount of one protein is kept constant and the other is increased, peaks associated with water bound to either protein can be identified. The hypothesis is that the more protein a sample contains, the more water proteins bind and the higher the peaks in the PSD graphs.

PSD below ice/water phase transition

Parameters used in PSD calculations were $T_0 = 273.15$ K, k = 89 nmK [14] (spherical pore) and $\delta = 0.8$ nm [10].

The first attempt was to find out at which range the calculated pore sizes vary. From Figure 6.9 it can be seen that the measured PSD range is from 2 nm to 50 nm. There is a very broad distribution between 5 nm and 50 nm and the protein associated peaks appear between 2 nm and 5 nm. To study the protein-related peaks, the smaller diameter range is focused from now on.

The PSDs of constant collagen and varying CS concentrations are shown in Figure 6.10 A and B and PSDs of constant CS and varying collagen in Figure 6.10 C and D. It can be clearly seen that there is a peak originating from eutectic phase transition

↓ Collagen | CS→	0 mg/g	5 mg/g	10 mg/g	20 mg/g
0 mg/g				X
10 mg/g				X
20 mg/g				X
40 mg/g	X	X	X	X X

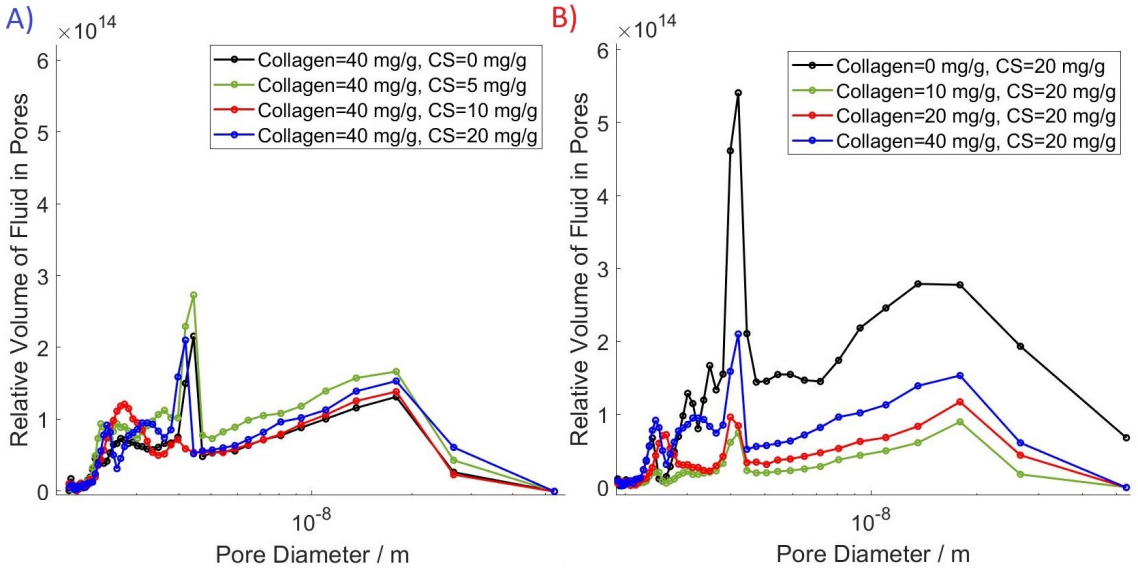

Figure 6.9: The measured pore size distribution range as a whole when both A) collagen and B) CS have maximum concentrations and $T_0 = 273.15$ K.

appearing at about 4 nm in each PSD graph. Depending on the sample, the location of the eutectic-related peak varies slightly around 4 nm. The peaks associated with protein content appear between 2 and 4 nm. The protein peaks have much weaker intensities compared to 4 nm peaks and it is possible that the 4 nm peaks are covering protein-related peaks.

It can be seen from Figure 6.10 A that when collagen concentration is 0 $\frac{\text{mg}}{\text{g}}$ and CS concentration increases, there are three peaks building up intensity at 2.3 nm, 2.9 nm and 3.3 nm. Correspondingly from Figure 6.10 C, it can be observed that when the concentration of CS is 0 $\frac{\text{mg}}{\text{g}}$ and collagen concentration increases, there are two peaks of 2.1 nm and 2.5 nm increasing in intensity. The zoomed PSDs of 0 $\frac{\text{mg}}{\text{g}}$ CS and collagen are represented in Figure 6.11. In Figures 6.10 B and D, there are PSDs of increasing protein content when collagen and CS have maximum concentrations. It can be noted that the pore diameters observed in graphs A and C appear also in these PSD graphs but the relationship of the peaks is not quite as clear as in the two previous graphs.

↓ Collagen | CS→	0 mg/g	5 mg/g	10 mg/g	20 mg/g
0 mg/g	X	X	X	X
10 mg/g	X			X
20 mg/g	X			X
40 mg/g	X	X	X	X

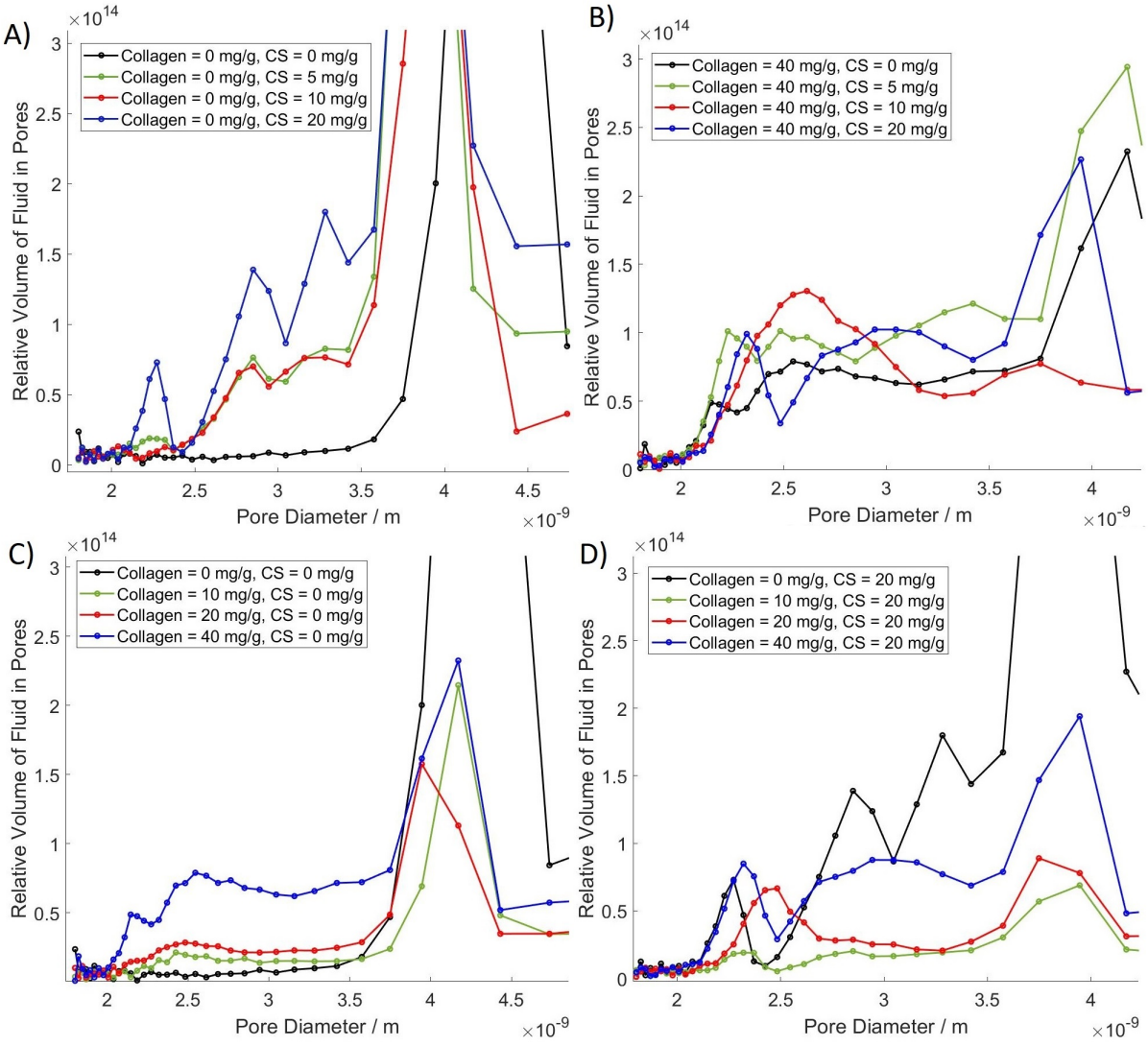

Figure 6.10: Effect of varying protein concentration on PSDs when A,B) collagen is constant and C,D) CS is constant and T_0=273.15 K.

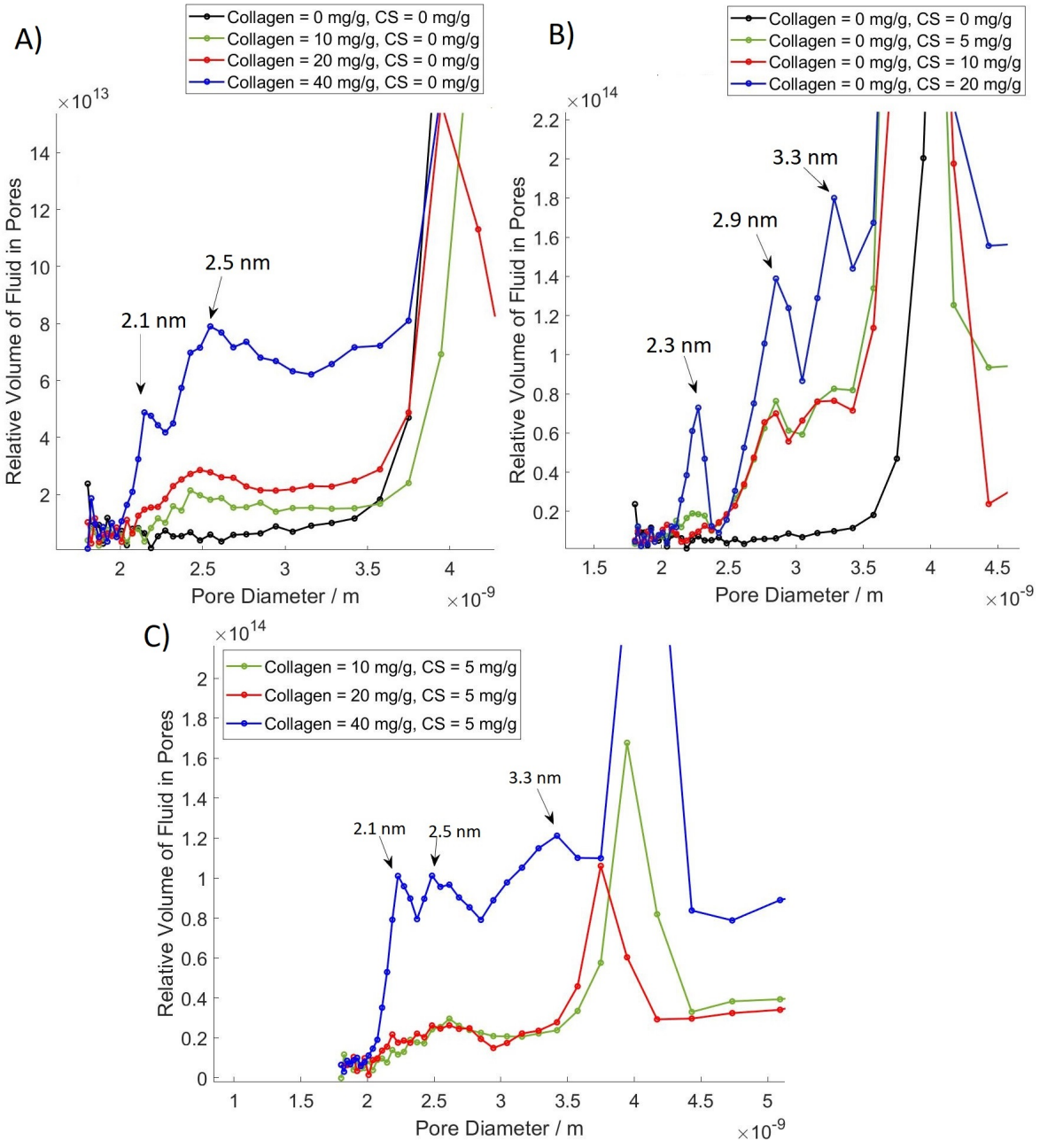

Figure 6.11: Zoomed PSDs of A) 0 $\frac{\text{mg}}{\text{g}}$ concentration of CS, B) 0 $\frac{\text{mg}}{\text{g}}$ concentration of collagen and C) a samples with mixed protein content.

The PSDs of samples with mixed protein concentrations are much more complex to interpret and the presence of large 4 nm peaks makes it even more complicated. It can be observed that the intensity of the protein peaks increase as the amount of protein increases but it is difficult to say which protein the peaks are associated with. In Figure 6.11 C is an example of a samples with mixed proteins from which protein related peaks can be identified. As the amount of collagen increases, the peaks of 2.1 nm and 2.5 nm increase in intensity as well. There is also a CS-related peak of 3.3 nm. However, from most of the graphs, such clear identification cannot be seen.

PSD below eutectic phase transition

The PSD calculations were repeated by changing the melting point of water to the eutectic point of PBS observed in Figure 6.2. The PSD parameters used were $T_0 = 246$ K, k=89 nmK [14] (spherical pore) and δ=0.8 nm [10].

The PSDs are represented in Figures 6.12. Now it can be seen that there are no peaks associated with eutectic phase transition and the protein-related peaks are more visible. The PSD graphs are much clearer but it must be taken into account that by changing the bulk melting temperature to the eutectic temperature, the graphs make up now only few percent of the total measured melting data and a fraction the signal left from the phase diagram and for that reason it is very likely that not all pore-related peaks are present.

Protein-related peaks can be seen especially clearly when collagen or CS have 0 $\frac{\text{mg}}{\text{g}}$ concentration and the concentration of the other protein increases (Figures 6.12 A and C). When collagen is kept 0 $\frac{\text{mg}}{\text{g}}$ and CS concentration increases, there are three peaks of 3 nm, 6 nm and 10 nm increasing in intensity. In case of 0 $\frac{\text{mg}}{\text{g}}$ CS and increasing collagen, there are two peaks of 3 nm and 4 nm increasing in intensity.

Now, it is much easier to identify peaks related to particular protein in PSDs of samples of mixed proteins. Peaks of 3 nm, 4 nm, 5 nm or 6 nm can be distinguished from almost all graphs. One example is shown in Figure 6.13: as the amount of collagen increases, the peaks of 3 nm, 4 nm and 5 nm increase in intensity. From the PSD of the sample containing maximum amount of both proteins, two clearly separated peaks of 3 nm and 5 nm can be observed. Thus, it can be said that the method is able to identify water associated with either protein also in the mixed protein gels.

↓ Collagen | CS→	0 mg/g	5 mg/g	10 mg/g	20 mg/g
0 mg/g	X	X	X	X
10 mg/g	X			X
20 mg/g	X			X
40 mg/g	X	X	X	X

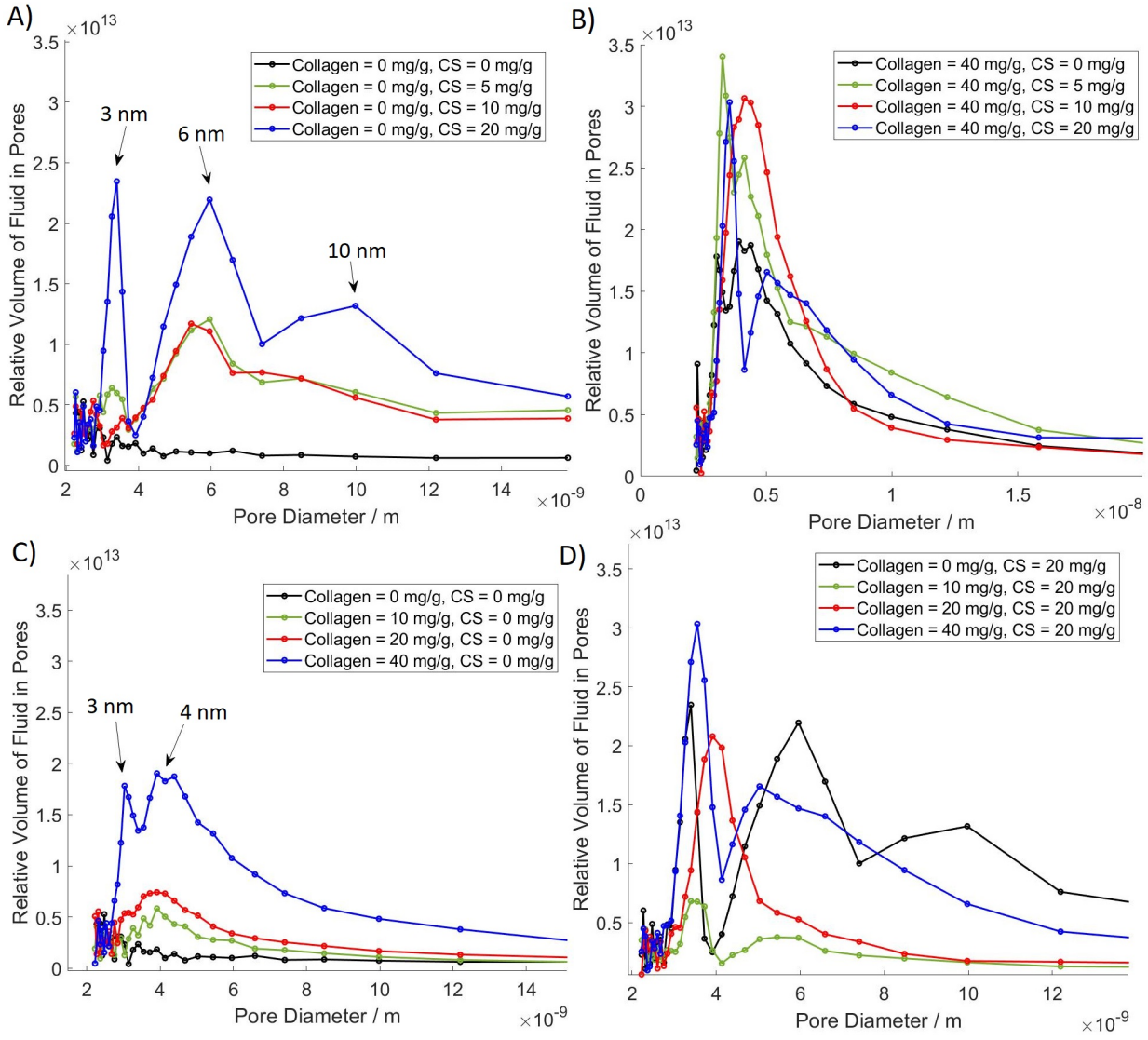

Figure 6.12: Effect of varying protein concentration on PSDs when A,B) collagen is constant and C,D) CS is constant and T_0=246 K.

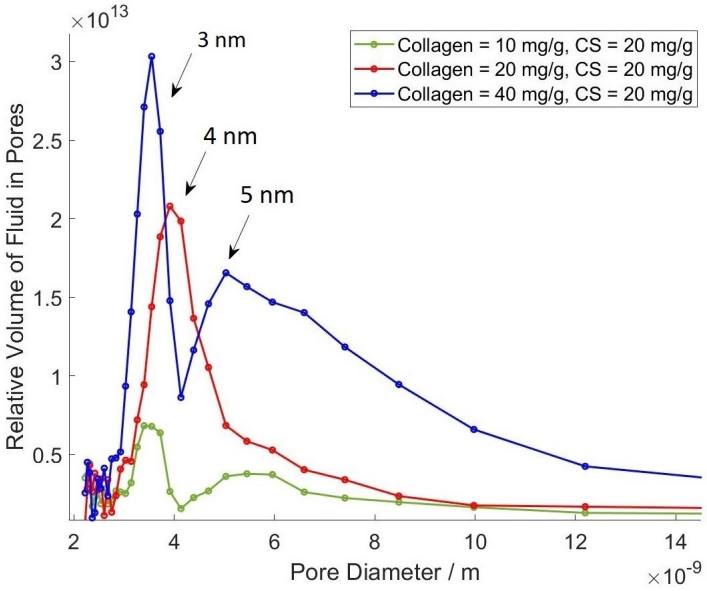

Figure 6.13: Effect of increasing protein content in mixed protein samples.

6.4.4 Effect of protein content on T_2 relaxation

One main research question was to study whether the T_2 relaxation time depend on protein content as a function of temperature. Of particular interest is whether there is a notable difference in T_2 at room temperature. The T_2 relaxation times were obtained from CPMG decay at each temperature step.

The graphs of T_2 relaxation as a function of temperature are shown in Figure 6.14. At low temperatures all samples show T_2 of 300 µs. At about 245 K T_2 starts to increase rapidly as the temperature increases ending up to around 1 s at room temperature. It can be observed that the amount of CS do not affect the T_2 but amount of collagen does. At low temperatures the T_2 dependence on collagen is not notable but at higher temperatures the smaller the amount of collagen the slower the T_2 relaxation. The difference in T_2 at room temperature is from 0.1 s to 1 s when collagen concentration decreases from 40 $\frac{\text{mg}}{\text{g}}$ to 0 $\frac{\text{mg}}{\text{g}}$.

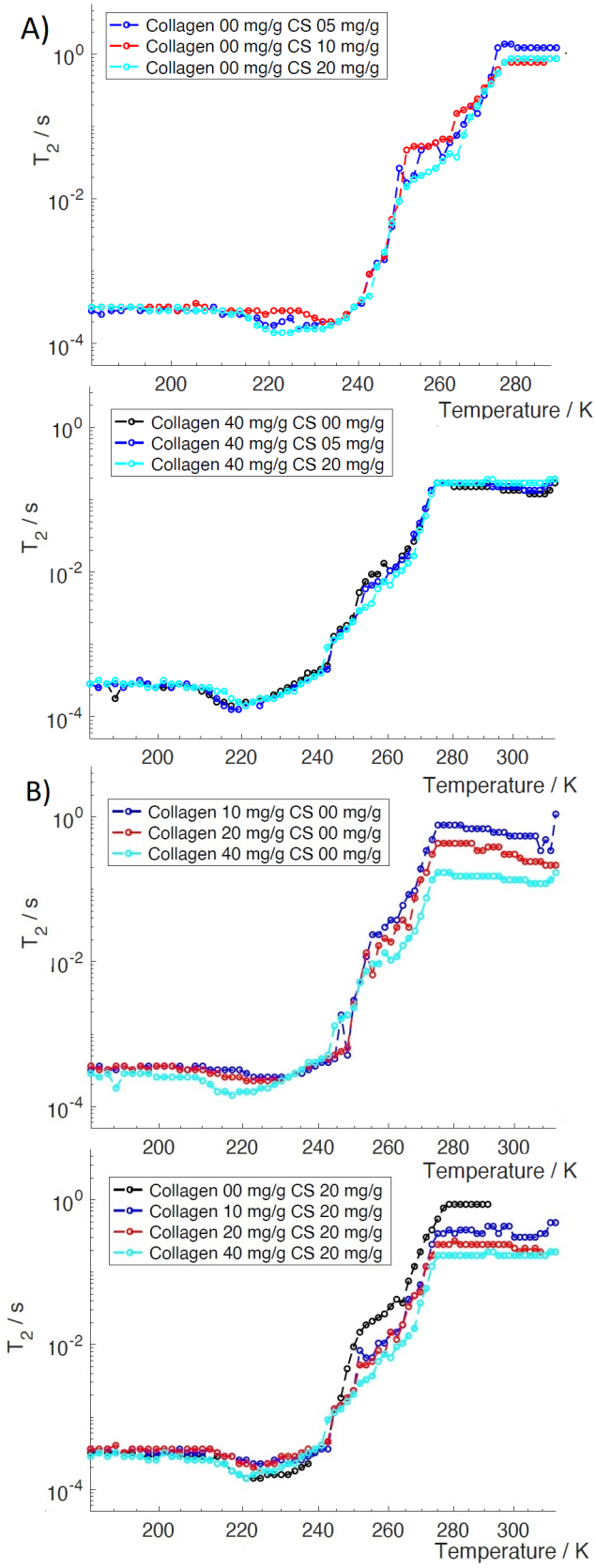

Figure 6.14: T_2 as a function of temperature when A) collagen and B) CS is kept constant.

Chapter 7

Discussion and Conclusions

The research consisted of three parts, the first two of which studied the phase transitions of salt solutions and porous materials, and the experimental results obtained from these parts were utilized in the final part to quantify the pore size distributions and measure the associated T_2 relaxation in articular cartilage model gels.

In the first part, we observed that both saline and phosphate-buffered saline show eutectic phase transition occurring at temperature range 242-250 K and bulk melting between 257-272 K. Both solutions show eutectic phase transition at temperatures below the theoretical equilibrium eutectic temperature of 252 K. Majda et al. (2017) [8] performed differential scanning calorimetry (DSC) with a 3.6 $\frac{g}{L}$ NaCl-water solutions and observed eutectic phase transition and bulk melting peaks clearly separated. In their measurements, the eutectic transition was more clearly noticeable than ours. They also found that below the bulk melting point, there is a wide distribution of melting temperatures but their eutectic phase transition appeared at a smaller range than ours. The slightly different results are due to the fact that NMRC and DSC are based on the measurement of different phenomena and the concentration of saline they used was higher than ours. Overall, the melting behaviour of salt solutions which we observed is in line with those reported by Majda.

From PSDs of saline and PBS, we observed that the melting signal originating from the eutectic phase transition produces a peak of 4 nm in PSD graph. There was also shown a wider distribution of pore sizes between 4-50 nm. Han et al. (2002 & 2004) [28,29] investigated freezing and melting of saline and PBS with DSC and cryomicroscopy. From DSC measurements, they observed that both saline and PBS show eutectic phase transition around 252 K. From cryomicroscope images, they observed

that after crystallization of water and hydrohalite, there is a space left between the ice crystals which produces a pore structure of its own. The broad melting temperature range below the bulk melting and corresponding PSD between 4-50 nm may be due to the melting of water in these ice crystal pores or the distribution of melting points as the NaCl concentration increases. When using a NaCl solution as a probe fluid, the eutectic-related and ice crystal peaks are problematic because they can obscure information about the pore structure of interest.

In the second part of the experiments, six silica bead samples imbibed with water or saline were studied. The PSD of silica samples imbibed with water showed peaks corresponding to each pore diameter but PSD of saline samples did not show exactly correct pore diameters. The same silica products and parameters were used so it can be seen that the solvent used has a clear effect on the melting behavior and PSD. Both water and silica samples showed smaller additional peaks at 2.5 nm and between 13-20 nm. These 2.5 nm peaks may originate from water melting on the silica bead surface because only silica samples show these but saline and PBS samples in the first part did not. The peaks of 13-20 nm originate from the distribution of melting points below bulk melting point. Both water and saline samples showed very similar melting behavior and no clear effect of eutectic transition was observed in the case of saline samples. It is possible that the eutectic transition occurs at wide temperature range and for that reason there was no clear signal increase of eutectic melting. Two saline samples showed tiny peaks between 3-4 nm which are possibly eutectic-associated peaks.

Since in the first part of the experiments it was found that the eutectic transition of salt solutions causes an extra peak and distorts actual pore sizes in the PSD, we repeated the changing of bulk melting point to the eutectic temperature. As a result, pore sizes above 4 nm are cut off and only 3.5 nm peaks are left. A change of the bulk melting point can thus eliminate, for example, the eutectic-related peak, but on the other hand also cut off some of the pore-related peaks. If the pore-related pore sizes are small enough, the change of bulk melting point can be advantageous but it also omits most of the melting data from the calculations. It was also found that when PSD was computed with lower bulk melting point, the calculated pore diameters shifted towards larger pore sizes. In order to keep the pore sizes at the same range, the k-value should also be recalibrated or it should be noted that the pore sizes calculated by this method may be larger than they actually are.

Rottreaua et al. (2018) performed cryoporometric measurements with silica and water as a probe liquid [17]. They used samples of three different types of silica and computed PSD from the water melting signal. They observed that the ice/water phase transition was smoother than in the case of our samples and there was only one peak for each sample in PSD and no additional peaks as in our PSDs. The better results are possibly due to better and longer lasting sample preparation.

It must also be noted that the choice of parameters used in PSD calculations is not entirely unambiguous [17]. The magnitude of the calibration constant k or thickness of non-freezing layer δ cannot be known with certainty in advance. In this study, we did not calibrate the k-value but used only values found in previous reports. For water as a cryoporometric probe liquid in spherical pores, the estimated k-values range between 42-106 nmK [14]. The values we have used in this study are 89 nmK and 96 nmK which fall within that estimated range. In case of silica samples, we could have calibrated the k-value with our own samples but ended up using the value 96 nmK calibrated by Majda [8]. They carried out DSC with five silica samples of different pore sizes filled with NaCl-water solution. Using melting point depression information from DSC profiles, they linearly fitted pore size as a function of inverse of melting point depression. Based on the Gibbs-Thomson equation, the slope of the fitted line is the calibrated k-value. The linear fitting includes three parameters from which the slope is the k-value of interest and the other two are related to interactions between imbibed liquid and pore walls. The disadvantage of linear fitting of Majda is that more samples should be measured to increase reliability because the fitting given by only five samples is not very stable. Rottreaua et al. [17] determined cryoporometric parameters with silica samples imbibed with water. They also used linear fitting but larger number of samples and found k-value of 99.1 nmK for spherical pores which is close to Majda's value. Their value was also verified with N_2 porosimetry and DSC which makes it very reliable. One simple way to calibrate the k-value is to do it visually using PSD graphs. If we change the values of k while observing at which value the PSD shows the corresponding pore diameters, the most suitable values for our samples are 95-100 nmK which is very close to calibrated values from linear fitting. The reported values for thickness of non-freezing layer for water in siliceous materials range between 0.3 and 2.6 nm [10]. The most studies suggest that the layer thickness is 1-3 water monolayers which corresponds to a thickness of 0.8 nm so we ended up choosing it as a layer thickness. The values of these two parameters are directly related

to the calculated pore size and changing them would also change the measured pore sizes. The reliability of the method could be improved if salt solutions were studied more extensively and the values of the parameters were better known.

On the basis of the results of first two parts of the experiments, the eutectic transition of the salt solution must be taken into account in the determination of the pore size distribution. The pore network, ice crystallization and increase of NaCl concentration at lower temperatures can cause additional peaks in the PSD. We observed that the solution has a major effect on pore size distribution and the same k-values do not work for salt solutions as with water. The eutectic-related peak can be eliminated by decreasing the bulk melting point, but on the other hand, the PSD is then calculated from only a few percent of the total melting data and then the PSD does not give actual pore sizes. Neither option provides a complete solution to the problem on its own but by combining the benefits of both methods, the information about pore sizes and peaks can be obtained.

In the third part of the experiments, the measured pore diameter range of protein gels was 2-50 nm. Between 5-50 nm, there was a very broad distribution of pore sizes, each sample showed a eutectic-related peak at 4 nm and between 2-4 nm a range of smaller peaks. A wide pore size range between 5-50 nm very likely originate from the distribution of melting points as the salt concentration increases [8]. We assumed that the smaller pore sizes originate from the protein-related water and for that reason, the pore sizes below the eutectic peak were focused on.

PSDs of protein gels were first calculated using the bulk melting point of water and then the observed eutectic temperature of PBS. In the first case, a few protein-related peaks were observed on the left side of the eutectic peak but the eutectic-related peak was so overbearing that it was almost impossible to conclude anything certain about the protein-related peaks because the peak very likely covered part of the desired protein-related peaks. In second case, the protein-associated peaks appeared more clearly but the distribution was calculated from data that accounted for only about 3 % of the total melting signal and for that reason, probably part of the essential melting data was left out of the calculations. The first case gives better information about the pore sizes and the latter case was found more useful in peak detection. As noted earlier, lowering the bulk melting point shifted the pore sizes to a larger area so it must be considered that in the latter case the pore sizes may not be correct.

The first PSD calculations resulted in protein-related pore sizes of 2.1-3.3 nm and the latter 3-10 nm. It is very likely that 4 nm eutectic peaks covered some of the peaks of interest. Although the pore sizes are different, the same peaks were identified from both PSD calculations. It should also be noted that we do not know exactly what the value of the calibration constant should be for these samples. Changing the value of the calibration constant changes the position of the peaks but despite that, actual pore sizes are very likely somewhere between 2-5 nm.

Combining these results obtained from these two cases, peaks characteristic for both proteins were observed. The intensity of the peaks increased as the amount of protein increased. When the amount of one protein was kept at 0 $\frac{\text{mg}}{\text{g}}$ and the amount of the other was increased, collagen-related peaks were observed between 2.1-2.5 nm and CS-related peaks between 2.3-3.3 nm. In case of mixed protein samples, the identification of the peaks associated with either protein was not as unambiguous but in the latter PSD calculations, the protein associated peaks were seen well enough to conclude that the method is able to detect protein-associated peaks in mixed protein samples as well.

In hydraulic permeability experiments, the pore diameter of articular cartilage has been estimated to be 4-6 nm [4]. Majda et al. measured pore side distributions of intact and degraded articular cartilage samples with differential scanning calorimetry [8] and found pore diameters of 11-14 nm. However, their lower limit of detection was 11 nm. In first case, we measured pore sizes of 2-4 nm which is consistent with the hydraulic permeability experiments. It must be taken into consideration that we did not use articular cartilage samples but models so the studies are not completely comparable. The position of eutectic-related peak was found around 4 nm and the location depended slightly on the sample which is also consistent with Majda et al. According to them, it is because negatively charged proteoglycans attract sodium which changes the salinity of the solution.

Saline or PBS as a cryoporometric solution have not been studied systematically and to our knowledge, Majda's report is the only one which utilizes calibration equation that takes into account the eutectic phase transition. The development of a calibration equation could make NMR cryoporometry a more practical method for determining pore sizes of biomaterials. Another possibility could be the elimination of eutectic phase transition by means of chemicals. Han et al. (2002) observed that the

addition of glycerol to PBS disappeared the eutectic phase transition in DSC profiles [29]. Glycerol is a liquid that occurs naturally in many biological systems so it could potentially be used in cryoporometry of biomaterials [20]. However, this would still leave the baseline issues caused by the melting point distribution of increasing NaCl concentrations.

NMR cryoporometry and differential scanning calorimetry are both methods of thermoporometry but NMRC is based on the different relaxation times of different states of matter while the DSC measures transient heat flows [9,10]. Relaxation times in NMR are related to molecular motion and transient heat flow to number and strength of molecular bonds. As the methods are based on the detection of different phenomena, differences in their results have also been observed. Jähnert et al. (2008) measured pore size distributions of silica nanopores with NMR cryoporometry and differential scanning calorimetry and compared the results [34]. They found out that NMRC was able to measure smaller pore sizes than DSC, phase transitions were observed at higher temperatures with NMRC than in DSC, and the phase transition ranges were wider with NMRC which consequently has an impact on computed pore size distributions. The results obtained by different thermoporometry methods cannot always be directly compared, but overall, it can be said that Majda's, Han's, and ours results have much the same features and can be compared with each other.

From the relaxation time measurements, we found that T_2 depends on the amount of collagen but not on the amount of CS at room temperature. We observed that the higher the collagen concentration, the shorter the T_2. Water in articular cartilage can be either free to move or bound to macromolecular binding sites. For that reason, articular cartilage may have many components of T_2 due to different environments [35]. Since articular cartilage has a layered structure and the orientation and density of the collagen fibres depend on cartilage zone, different zones have different relaxation times. In superficial and deep zones, the collagen fibres are closely packed and in middle zone sparsely spread and unorganized and consequently the T_2 on deep and superficial zones are shorter than in middle zone [32]. The layered structure also causes the orientation of the articular cartilage relative to the external field to matter: it has been found that when the orientation of the collagen fibres is changed to a magical angle with respect to the field, the amount of T_2 components is reduced from two to one [36]. For these reasons, the determination of articular cartilage T_2 is not straigthforward.

However, out attempt was to see if we can distinguish a relation between cartilage model protein content and T_2 by NMR cryoporometry. We observed that at low temperatures, there is no significant impact on either protein in T_2 but close to room temperature, the T_2 is dependent on collagen but not on chondroitin sulfate. There are plenty of previous studies that have investigated the effect of collagen and proteoglycans on articular cartilage relaxation times. Since the amount of collagen and proteoglycans is also associated with cartilage degradation and osteoarthritis, T_2 have also been studied in relation to different stages cartilage degeneration. Nieminen et al. (2000 & 2001) used magnetic resonance techniques to articular cartilage and concluded that T_2 follow the collagen fibril orientation in different zones of cartilage and thus is shortest in zones where collagen density is highest [32]. They also found that collagen degradation increased T_2 in cartilage [37]. In both studies, they observed that proteoglycans had no significant impact on T_2. Our results also seem to be in line with the fact that T_2 is not very sensitive to the amount of proteoglycans. It is possible that T_2 is not sensitive to the amount of proteoglycans because water molecules are so loosely bound to them or proteoglycans are saturated with sodium ions [8]. However, information on the proteoglycan content can be obtained, for example, by contrast agent T_1 imaging to provide an overall picture of the protein content in the articular cartilage [31]. Overall, the articular cartilage models we used are very simple compared to the complex structure of real articular cartilages, and we cannot compare them directly but the models can allow, for example, the detailed study of relaxation and dynamic processes of water molecules in environment of cartilage proteins with help of NMR methods.

Altogether, although our method does not accurately determine the pore size of articular cartilage models, it can be concluded that the method is able to identify water associated with proteoglycans and collagen in articular cartilage. Thermoporometry and phase transitions of salt solutions are unexplored disciplines and their development may open up new perspectives for biomaterial research. The methods of NMR and thermoporometry provide new insights into water of articular cartilage which may provide new approaches for diagnosis of cartilage degenerative diseases.

References

[1] Fox AJS, Bedi A, Rodeo SA. The basic science of articular cartilage: structure, composition and function. Sports health. 2009; 1(6): 461–468.

[2] Medvedeva EV, Grebenik EA, Gornostaeva SN, Telpuhov VI, Lychagin AV et al. Repair of damaged articular cartilage: current approaches and future directions. International journal of molecular sciences. 2018; 19(8): 2366.

[3] Hunter W. Of the structure and disease of articulating cartilages. Clinical orthopaedics and related research. 1743. Published online 1995; (317): 3-6.

[4] Mow VC, Ratcliffe A, Poole AR. Cartilage and diarthrodial joints as paradigms for hierarchical materials and structures. Biomaterials. 1992; 13(2): 67-97.

[5] Telkki V. 761359A Spectroscopic methods, NMR spectroscopy. University of Oulu. Lecture material 2018. In Finnish.

[6] Gold GE, Chen CA, Koo S, Hargreaves BA, Bangerter NK. Recent advances in MRI of articular cartilage. AJR Am J Roentgenol. 2009; 193(3):628-638.

[7] Bhosale A, Richardson J. Articular cartilage: structure, injuries and review of management. British medical bulletin. 2008; 87(1): 77-95.

[8] Majda D, Bhattarai A, Riikonen J, Napruszewska BD, Zimowska M, Michalik-Zym A et al. New approach for determining cartilage pore size distribution: NaCl-thermoporometry. Microporous and mesoporous materials. 2017; 241(15): 238-245.

[9] Mitchell J, Webber JBW, Strange JH. Nuclear magnetic resonance cryoporometry. Physics reports. 2008; 461(1): 1–36.

[10] Riikonen J, Salonen J, Lehto V-P. Utilising thermoporometry to obtain new insights into nanostructured materials review part 1. Journal of thermal analysis and calorimetry. 2011; 105: 811-821.

[11] Keeler J. Understanding NMR spectroscopy. Second edition. John Wiley & Sons; 2010.

[12] Kantola A, Telkki V. 766666S NMR spectroscopy. University of Oulu. Lecture material 2020.

[13] Loria JP, Rance M, Palmer AG. A relaxation-compensated Carr-Purcell-Meiboom-Gill sequence for characterizing chemical exchange by NMR spectroscopy. Journal of the American chemical society. 1999; 121(10): 2331–2332.

[14] Petrov O, Furo I. NMR cryoporometry: principles, applications and potential. Progress in nuclear magnetic resonance spectroscopy. 2009; 54(2): 97–122.

[15] Riikonen J, Salonen J, Lehto V-P. Utilising thermoporometry to obtain new insights into nanostructured materials review part 2. Journal of thermal analysis and calorimetry. 2011; 105: 823-830.

[16] Indekeu JO. Introduction to wetting phenomena. Acta physica polonica series B. 1995; 26(6): 1065-1100.

[17] Rottreaua TJ, Parlett CMA, Lee AF, Evans R. NMR cryoporometric measurements of porous silica: a method for the determination of melting point depression parameters of probe liquids. Microporous and mesoporous materials. 2018; 264(1): 265-271.

[18] Petrov O, Furo I. A study of freezing–melting hysteresis of water in different porous materials. Part I: porous silica glasses. Microporous and mesoporous materials. 2011; 138(1-3): 221-227.

[19] Petrov O, Furo I. Curvature-dependent metastability of the solid phase and the freezing-melting hysteresis in pores. Physical review. 2006; 73(1): 011608.

[20] Gordon Betts J, Desaix P, Johnson E, Johnson JE, Korol O, Kruse D et al. Anatomy and physiology. Rice University. OpenStax; 2013. https://openstax.org/details/books/anatomy-and-physiology

[21] Mow VC, Holmes MH, Lai WM. Fluid transport and mechanical properties of articular cartilage: A review. Journal of biomechanics. 1984: 17(5): 377-394.

[22] Stockwell RA. Chondrocytes. Journal of clinical pathology. 1978; 12: 7-13.

[23] Buckwalter JA, Mankin HJ, Grodzinsky AJ. Articular cartilage and osteoarthritis. AAOS instructional course lectures. 2005; 54: 465-80.

[24] Hunter DJ, Felson DT. Osteoarthritis. BMJ. 2006; 332(7542): 639-642.

[25] Buckwalter JA, Mow VC, Ratcliffe A. Restoration of injured or degenerated articular cartilage. Journal of the American academy of orthopaedic surgeons. 1994; 2(4): 192-201.

[26] PBS (Phosphate Buffered Saline) (1X, pH 7.4) Preparation. AAT Bioquest. (Cited 1.4.2021) https://www.aatbio.com/resources/buffer-preparations-and-recipes/pbs-phosphate-buffered-saline

[27] Sarbu I, Sebarchievici C. Solar heating and cooling systems: fundamentals, experiments and applications. 1st edition. Amsterdam, [Netherlands]: academic press, 2017.

[28] Han B, Bischof JC. Thermodynamic nonequilibrium phase change behavior and thermal properties of biological solutions for cryobiology applications. Journal of biomechanical engineering. 2004; 126(2): 196-203.

[29] Han B, Devireddy RV, Bischof JC. Phase change behavior of biomedically relevant solutions. Proceedings of the ASME 2002 international mechanical engineering congress and exposition. Advances in bioengineering. New Orleans, Louisiana, USA. 2002: 67-75.

[30] Swenne DA. The eutectic crystallization of NaCl2H2O and ice. 1983. Technische hogeschool Eindhoven.

[31] Nissi MJ, Töyräs J, Laasanen MS, Rieppo J, Saarakkala S, Lappalainen R, Jurvelin JS, Nieminen MT. Proteoglycan and collagen sensitive MRI evaluation of normal and degenerated articular cartilage. Journal of orthopaedic research. 2004; 22(3): 557-64.

[32] Nieminen MT, Rieppo J, Töyräs J, Hakumäki JM, Silvennoinen J, Hyttinen MM, Helminen HJ, Jurvelin JS. T_2 relaxation reveals spatial collagen architecture in articular cartilage: a comparative quantitative MRI and polarized light microscopic study. Magnetic resonance in medicine. 2001; 46(3): 487-93.

[33] Dunn TC, Lu Y, Jin H, Ries MD, Majumdar S. T2 relaxation time of cartilage at MR imaging: comparison with severity of knee osteoarthritis. Radiology. 2004; 232(2): 592-8.

[34] Jähnert S, Chávez FV, Schaumann GE, Schreiber A, Schönhoff M, Findenegg G. Melting and freezing of water in cylindrical silica nanopores. Physical chemistry chemical physics. 2008; 10: 6039-51.

[35] Wang N, Xia Y. Experimental issues in the measurement of multi-component relaxation times in articular cartilage by microscopic MRI. Journal of magnetic resonance. 2013; 235: 15-25.

[36] Xia Y. Magic-angle effect in magnetic resonance imaging of articular cartilage: a review. Investigative radiology. 2000; 35(10): 602-21.

[37] Nieminen MT, Töyräs J, Rieppo J, Hakumäki JM, Silvennoinen J, Helminen HJ, Jurvelin JS. Quantitative MR microscopy of enzymatically degraded articular cartilage. Magnetic resonance in medicine. 2000; 43(5): 676-81.